Interception of two spherical drops in linear Stokes flow

C. Pozrikidis

Abstract   A boundary-integral method is developed for computing the interception of two spherical drops with arbitrary radii and viscosities in infinite linear Stokes flow. At any instant, the flow is computed in a frame of reference with origin at the center of one drop, using a cylindrical polar coordinate system whose axis of revolution passes through the center of the second drop. Taking advantage of the axial symmetry of the interfaces in the drop coordinates, the problem is formulated as a system of integral equations for the zeroth, first, and second Fourier coefficients of the normal component of the jump in the interfacial traction and for the meridional and azimuthal components of the interfacial velocity with respect to the meridional angle. The integral equations are solved with high accuracy using a boundary-element method featuring adaptive boundary-element distribution and automatic time-step adjustment according to the interfacial gap. Simulations of two drops intercepting in uniaxial straining flow provide accurate data on the drop collision velocity and particle stress tensor for gaps as small as 10^{-4} times the drop radius. Simulations of two drops intercepting in simple shear flow confirm that slightly offset drops collide during the interception. Accurate data are presented for Batchelor's relative mobility functions in linear Stokes flow used to describe the relative droplet motion.

Keywords   Boundary-integral method · Bubbles · Drops · Stokes flow

1 Introduction

Small droplets and bubbles suspended in an ambient liquid are common constituents of biological, industrial, and environmental fluids. Numerous studies of droplet and bubble motion have been conducted in order to assess the nature and magnitude of the flow-induced deformation in shear and elongational flow; establish thresholds for breakup; illustrate particle trajectories; determine the motion near boundaries; investigate the process of sedimentation; determine the collision efficiency and thereby assess the stability of the suspended phase under a broad range of flow conditions. In recent years, droplet and bubble motion has received considerable attention due to potential applications in microfluidics.

Because droplets and bubbles encountered in practice are typically small, the flow around them occurs at small Reynolds numbers even in the case of a turbulent ambient flow. The hydrodynamic interaction of particles, liquid

C. Pozrikidis (✉)
Department of Chemical Engineering, University of Massachusetts, Amherst, MA 01003, USA
e-mail: cpozrikidis@ecs.umass.edu

drops, and gas bubbles in Stokes flow has been investigated extensively by asymptotic and numerical methods, as reviewed by Kim and Karrila [1]. Batchelor and Green [2,3] discussed the motion of two freely suspended spherical particles in infinite linear flow and developed asymptotic and numerical solutions for remote and nearly touching particles. Zinchenko [4–7] studied the interaction of two closely spaced spherical drops and investigated the rheological properties of a dilute suspension. Zhang and Davis [8] derived analytical expressions for the mobility functions of two remote drops and presented numerical results for arbitrary separations. Wang et al. [9] combined these results into a highly accurate scheme that allowed them to integrate the equations governing the relative drop motion, and thus determine the droplet collision efficiency by trajectory analysis in uniaxial straining and simple shear flow. Fuentes et al. [10,11] developed asymptotic expansions for the mobility of a small drop near a larger drop. Other authors have conducted numerical simulations of drop interception by boundary-element methods, as reviewed by Zinchenko and Davis [12]. While these methods are powerful when significant deformation occurs, the governing equations become extremely stiff in the limit of vanishing deformation where surface tension plays a dominant role.

The capillary number is a dimensionless parameter expressing the relative importance of the deforming hydrodynamic stresses and the restoring capillary stresses due to surface tension,. The assumption of spherical bubble and drop interfaces is accurate in the limit of zero capillary number and when the drop or bubble interfaces are separated by a sufficiently large gap. When the minimum separation becomes comparable to the capillary number, interfacial deformation occurs yielding a two-sided dimple that may prevent collision leading to coalescence. In the absence of interfacial deformation, spherical interfaces make contact at a finite time provided that the contact force pressing the drops against each another is sufficiently strong and persist for a sufficiently long period of time. Zinchenko and Davis [12] pointed out that the condition of small capillary number does not generally warrant the neglect of deformation. The reason is that interfacial deflection acts as a singular perturbation preventing the interfaces from touching in the absence of attractive intermolecular force fields. In the case of two drops pressing against one another in an axisymmetric uniaxial elongational flow, interfacial deformation has been shown to undoubtedly prevent collision. Recent boundary-integral computations [12] have confirmed that this is also true in the case of drops intercepting obliquely in simple shear flow. The numerical results have shown that the minimum interfacial gap developing during the strong interaction and near-collision phase scales with a positive power of the capillary number. However, the effect of interfacial deformation becomes irrelevant in the limit of zero capillary numbers where attractive intermolecular forces of non-hydrodynamic origin cause spherical interfaces to coalescence for sufficiently small gaps. The study of spherical drops and bubbles is relevant to microfluidics where the capillary number is miniscule.

In this paper, a boundary-integral method is developed for computing the motion of two spherical liquid drops suspended in infinite linear Stokes flow, in the limit of zero capillary number. Given the instantaneous relative drop position, we compute the flow in a frame of reference with origin at the center of one drop using a cylindrical polar coordinate system whose axis of revolution passes through the center of the second drop. The problem is formulated as a system of integral equations for the zeroth, first, and second Fourier coefficients of the normal component of the interfacial traction jump and interfacial velocity with respect to the meridional angle. The integral equations are solved with high accuracy using a boundary-element method featuring adaptive element distribution and automatic time-step adjustment according to the interfacial gap. The results are in excellent agreement with those obtained previously by Zinchenko, Davis and coworkers using functional expansion and asymptotic methods for large and small separations, and provide an alternative venue for describing the motion of drops consisting of the same or different fluids.

2 Problem statement and mathematical formulation

We consider slow viscous flow past two neutrally buoyant liquid drops suspended in an effectively infinite ambient fluid, as shown in Fig. 1. The ambient fluid is denoted by the index 1, the first drop is denoted by the index 2, and the second drop is denoted by the index 3. Far from the drops, the velocity obtains the linear form

Fig. 1 Two spherical drops with arbitrary radii intercept in a linear flow; (X, Y, Z) are the global coordinates fixed at the laboratory frame, (x, y, z) are particle doublet coordinates, (r, θ, φ) are corresponding spherical polar coordinates, and (x, σ, φ) are cylindrical polar coordinates attached to one drop
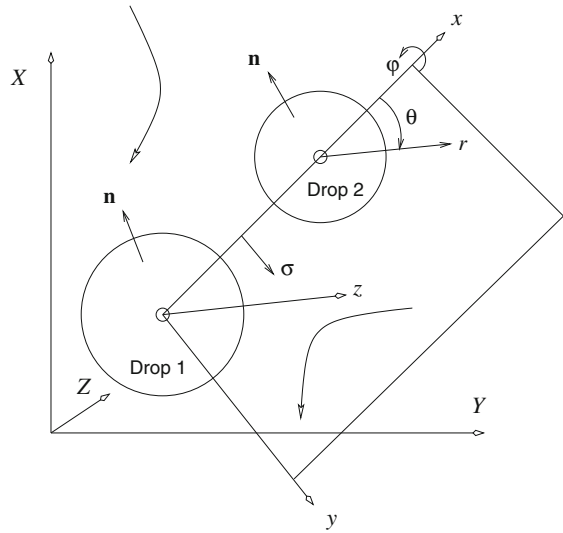
$$\mathbf{U}^\infty(\mathbf{X}) = \mathbf{L}^T \cdot \mathbf{X},$$ (2.1)

where $\mathbf{L} = \nabla \mathbf{U}^\infty$ is the velocity gradient tensor, the superscript T denotes the matrix transpose, $\mathbf{X}$ is the position vector, and $\mathbf{U}$ is the velocity in laboratory-fixed coordinates. The equivalent spherical radius of the first drop is $R = a$ and the equivalent spherical radius of the second drop is $R = \delta a$, where δ is the radius ratio; both are defined such that the volume of each drop is $\frac{4\pi}{3} R^3$. Without loss of generality, we will assume that the first drop is larger than the second drop, $\delta \leq 1$.

The Reynolds number of the flow around the drops is defined as $\text{Re} = U a \rho_1 / \mu_1$, where U is a characteristic velocity, ρ is the density, and μ is the viscosity. In physical applications of interest, the Reynolds number is so small that the flow is governed by the linear equations of Stokes flow, including the Stokes equation and the continuity equation,

$$-\nabla P + \mu_i \nabla^2 \mathbf{U} = \mathbf{0}, \quad \nabla \cdot \mathbf{U} = 0,$$ (2.2)

for $i = 1, 2, 3$, where P is the dynamic pressure incorporating hydrostatic variations. The velocity is continuous across the interface of each drop, but the interfacial traction undergoes a discontinuity determined by the surface tension, γ,

$$\Delta \mathbf{F} \equiv \Delta \boldsymbol{\Sigma} \cdot \mathbf{N} = 2\kappa_m \gamma \, \mathbf{N},$$ (2.3)

where $\boldsymbol{\Sigma}$ is the Newtonian stress tensor, $\mathbf{N}$ is the unit vector normal to the drop surface pointing into the ambient fluid, κ_m is the mean curvature reckoned to be positive for a sphere, and $\Delta q \equiv q_1 - q_i$ denotes the interfacial jump of a generic variable q, for $i = 2, 3$. To simplify the notation, we have assumed that the interfaces exhibit the same surface tension.

2.1 Asymptotics for small capillary numbers

It is useful to decompose the velocity and pressure fields in each fluid into a capillary component (C), a base component (B), and a disturbance component (D),

$$\mathbf{U} = \mathbf{U}^B + \mathbf{U}^D, \quad P = P^C + P^B + P^D.$$ (2.4)

Outside the drops, the capillary component vanishes and the base component represents the incident linear flow,

$$p^{C,1} = 0, \quad \mathbf{U}^{B,1} = \mathbf{U}^{\infty}, \quad p^{B,1} = P_0, \tag{2.5}$$

where P_0 is a constant ambient pressure. Inside the first drop, the capillary pressure is given by Laplace's law for a spherical drop, and the base component represents the continuation of the incident shear flow,

$$P^{C,2} = 2\frac{\gamma}{a}, \quad \mathbf{U}^{B,2} = \frac{\mu_1}{\mu_2}\mathbf{U}^{\infty}, \quad P^{B,2} = P_0. \tag{2.6}$$

Similar expressions are written for the second drop,

$$P^{C,3} = 2\frac{\gamma}{\delta a}, \quad \mathbf{U}^{B,3} = \frac{\mu_1}{\mu_3}\mathbf{U}^{\infty}, \quad P^{B,3} = P_0. \tag{2.7}$$

Corresponding base and disturbance velocity and pressure fields satisfy the equations of unforced Stokes flow. Near the drops, the base and disturbance flows have comparable magnitudes. When the fluid viscosities are different, the base velocity field is discontinuous across the drop interfaces. In contrast, the base stress field is spatially uniform and continuous throughout the domain of flow, irrespective of the fluid viscosities. The stress field associated with the capillary pressure undergoes a discontinuity across the interfaces.

We confine our attention to situations where the surface tension is strong enough to prevent significant deformation of the interfaces from the spherical shape against the deforming action of the stresses imparted by the incident flow. The formal requirement is that the capillary number, $\mathrm{Ca} = \mu_1 U/\gamma$, is sufficiently small. The disturbance velocity and stress fields can be expanded in perturbation series with respect to Ca whose leading terms are

$$\mathbf{U} = \mathbf{U}^B + \mathbf{U}^{D(0)} + \mathrm{Ca}\,\mathbf{U}^{D(1)}, \qquad \mathbf{\Sigma} = \mathbf{\Sigma}^C + \mathbf{\Sigma}^B + \mathbf{\Sigma}^{D(0)} + \mathrm{Ca}\,\mathbf{\Sigma}^{D(1)}. \tag{2.8}$$

The isotropic capillary stress tensor, $\mathbf{\Sigma}^C$ is defined with respect to the capillary pressure of the spherical drops.

The surface of each drop can be described by the similar asymptotic expansion

$$\frac{r}{R} = 1 + \mathrm{Ca}\,\phi(\theta, \varphi), \tag{2.9}$$

where r is the distance from the drop center, the dimensionless function $\phi(\theta, \varphi)$ describes the deformed shape to leading order with respect the capillary number, and (r, θ, φ) comprises a system of spherical polar coordinates attached to each drop, as shown in Fig. 1. The unit vector normal to the drop surfaces can be expanded in a similar fashion as

$$\mathbf{N} = \mathbf{e}_r + \mathrm{Ca}\,\mathbf{N}^{(1)}, \tag{2.10}$$

where $\mathbf{e}_r$ is the radial unit vector, and the superscript (1) signifies ordering with respect to the capillary number. Requiring $|\mathbf{N}|^2 = \mathbf{N} \cdot \mathbf{N} = 1$ and substituting (2.10) yields $\mathbf{e}_r \cdot \mathbf{N}^{(1)} = 0$ to first order in the capillary number, which shows that $\mathbf{N}^{(1)}$ is a tangential but not a unit vector. Now substituting $F = r - R\,[1 + \mathrm{Ca}\,\phi(\theta, \varphi)\,]$ in the expression for the normal vector, $\mathbf{N} = \nabla F/|\nabla F|$, and linearizing with respect to Ca, we find $\mathbf{N}^{(1)} = -\nabla\phi$.

The mean curvature of a drop interface can be similarly expanded with respect to the capillary number,

$$\kappa_m = \frac{1}{R} + \mathrm{Ca}\,\kappa_m^{(1)}, \tag{2.11}$$

where

$$\kappa_m^{(1)} = -\frac{1}{2R}\left(2\phi + \cot\theta\,\frac{\partial\phi}{\partial\theta} + \frac{\partial^2\phi}{\partial\theta^2} + \frac{1}{\sin^2\theta}\,\frac{\partial^2\phi}{\partial\varphi^2}\right); \tag{2.12}$$

e.g., [13, p. 162]. If the first-order curvature, $\kappa_m^{(1)}$, is known, this expression provides us with a partial differential equation for the interfacial deformation, $\phi(\theta, \varphi)$.

In a frame of reference translating with the drop velocity, $\mathbf{V}$, the spherical drop surface appears stationary and the relative normal velocity is zero. Substituting the perturbation expansions for the velocity and normal vector in the interfacial condition $\mathbf{U} \cdot \mathbf{N} = \mathbf{V} \cdot \mathbf{N}$, we find

$$(\mathbf{U}^B + \mathbf{U}^{D(0)}) \cdot \mathbf{e}_r = \mathbf{V} \cdot \mathbf{e}_r \tag{2.13}$$

evaluated on either side of the undeformed interface, $r = R$, with an error on the order of Ca.

Next, we consider the dynamic interfacial condition $\Delta \boldsymbol{\Sigma} \cdot \mathbf{N} = 2\kappa_m \gamma \mathbf{N}$. Substituting the perturbation expansion for the stress and noting that $\Delta \boldsymbol{\Sigma}^B = \mathbf{0}$, we find

$$2\frac{\gamma}{R}\mathbf{N} + \Delta \boldsymbol{\Sigma}^{D(0)} \cdot \mathbf{N} = 2\kappa_m \gamma \mathbf{N}, \tag{2.14}$$

with an error on the order of Ca. Substituting the asymptotic expansions for the normal vector and mean curvature, and expressing the surface tension in terms of the capillary number on the right-hand side, we find

$$\Delta \mathbf{F}^{D(0)} \equiv \Delta \boldsymbol{\Sigma}^{D(0)} \cdot \mathbf{e}_r = 2\mu_1 U \, \kappa_m^{(1)} \, \mathbf{e}_r, \tag{2.15}$$

with an error on the order of Ca, where all terms are evaluated at the position of the unperturbed interface, $r = R$. The normal and tangential components of the jump in the interfacial traction are

$$\Delta F_r^{D(0)} \equiv \Delta \mathbf{F}^{D(0)} \cdot \mathbf{e}_r = 2\mu_1 U \kappa_m^{(1)}, \quad \mathbf{e}_r \times \Delta \mathbf{F}^{D(0)} \times \mathbf{e}_r = \mathbf{0}. \tag{2.16}$$

To leading order, the force exerted on each drop is

$$\mathbf{F} = \iint\limits_D \Delta f_r^{D(0)} \, \mathbf{e}_r \, \mathrm{d}S, \tag{2.17}$$

where the integration is performed over the spherical interface. In the case of freely suspended drops, the drop velocity, $\mathbf{V}$, should be such that the force is zero. The torque with respect to the center of the spherical drop is identically zero.

The motion of the center of the drop, $\mathbf{X}_c$, is governed by the ordinary differential equation

$$\frac{\mathrm{d}\mathbf{X}_c}{\mathrm{d}t} = \mathbf{V}. \tag{2.18}$$

Similar equations can be written for the second drop.

We have formally derived Taylor's [14] boundary conditions for the normal component of the velocity of the leading-order flow, and demonstrated that the tangential components of the leading-order traction is zero over the spherical interfaces. This kinematic condition replaces the usual dynamic condition requiring that the normal component of the jump in traction is balanced by the capillary force due to surface tension. In addition, we have derived an expression for the normal component of the leading-order traction in terms of the first-order mean curvature, $\kappa_m^{(1)}$.

The computational task has been reduced to solving the Stokes flow problem for the tangential velocity components and jump in the normal component of the traction across the interfaces. Once this has been accomplished, the first-order curvature, $\kappa_m^{(1)}$, can be recovered from the normal interfacial force balance, and the first-order correction to the interfacial shape can be computed by solving the differential equation

$$2\phi + \cot\theta \, \frac{\partial\phi}{\partial\theta} + \frac{\partial^2\phi}{\partial\theta^2} + \frac{1}{\sin^2\theta} \frac{\partial^2\phi}{\partial\varphi^2} = -\frac{R}{\mu_1 U} \Delta F_r^{D(0)}, \tag{2.19}$$

where the left-hand side is a known. A solution of the homogeneous equation expressing translation along the X-axis is $\phi = \cos\theta$. Solutions of the homogeneous equation expressing translation along the Y- or Z-axis are $\phi = \sin\theta\cos\varphi$ and $\phi = \sin\theta\sin\varphi$.

The superscript (0) is now suppressed, and the disturbance flow is tacitly identified with its leading-order component.

2.2 Drop doublet coordinates

It is convenient to recast the problem into a standard form by introducing a new coordinate system, (x, y, z), with origin at the center of the first drop, $\mathbf{X}_c^{(1)}$. The x-axis passes through the centers of the two drops, and the y- and z-axes point in two orthogonal but otherwise unspecified directions. Thus, defining the particle coordinate system

affords one degree of freedom. The position vector, $\mathbf{x}$, and velocity, $\mathbf{u}$, in the particle coordinates transform according to the equations

$$\mathbf{X} = \mathbf{X}_c^{(1)} + \mathbf{A} \cdot \mathbf{x}, \quad \mathbf{U} = \mathbf{A} \cdot \mathbf{u}. \tag{2.20}$$

$\mathbf{A}$ is an orthogonal transformation matrix whose columns are the direction cosines of the unit vectors along the x, y, and z-axes,

$$\mathbf{A} = \begin{bmatrix} (\mathbf{e}_x)_X & (\mathbf{e}_y)_X & (\mathbf{e}_z)_X \\ (\mathbf{e}_x)_Y & (\mathbf{e}_y)_Y & (\mathbf{e}_z)_Y \\ (\mathbf{e}_x)_Z & (\mathbf{e}_y)_Z & (\mathbf{e}_z)_Z \end{bmatrix} \equiv \begin{bmatrix} A_{Xx} & A_{Xy} & A_{Xz} \\ A_{Yx} & A_{Yy} & A_{Yz} \\ A_{Zx} & A_{Zy} & A_{Zz} \end{bmatrix}, \tag{2.21}$$

where

$$\mathbf{e}_x = \frac{\mathbf{X}_c^{(2)} - \mathbf{X}_c^{(1)}}{|\mathbf{X}_c^{(2)} - \mathbf{X}_c^{(1)}|}, \quad \mathbf{e}_i \cdot \mathbf{e}_j = \delta_{ij}. \tag{2.22}$$

Applying the velocity transformation rules for the incident linear flow, we derive an expression for the velocity in the particle-fixed coordinates,

$$\mathbf{u}^\infty(\mathbf{x}) = \mathbf{A}^T \cdot \mathbf{L}^T \cdot \mathbf{X} = \mathbf{A}^T \cdot \mathbf{L}^T \cdot (\mathbf{X}_c^{(1)} + \mathbf{A} \cdot \mathbf{x}), \tag{2.23}$$

which can be restated as

$$\mathbf{u}^\infty(\mathbf{x}) = \mathbf{v}^\infty + \mathbf{M}^T \cdot \mathbf{x}, \tag{2.24}$$

where

$$\mathbf{v}^\infty = \mathbf{A}^T \cdot \mathbf{L}^T \cdot \mathbf{X}_c^{(1)}, \quad \mathbf{M} = \mathbf{A}^T \cdot \mathbf{L} \cdot \mathbf{A}. \tag{2.25}$$

The matrix $\mathbf{M}$ is the velocity gradient tensor in the particle-fixed coordinates. The orthogonality of the matrix $\mathbf{A}$ ensures that the trace of $\mathbf{M}$ is zero.

Next, we introduce cylindrical polar coordinates (x, σ, φ) complementary to the working spherical polar coordinates shown in Fig. 1, where σ is the distance from the x-axis, and the meridional angle φ is defined such that $y = \sigma \cos \varphi$ and $z = \sigma \sin \varphi$. The kinematic boundary condition (2.13) on the surface of each drop requires

$$u_r = \mathbf{A}^T \cdot \mathbf{V} \cdot \mathbf{n} = \mathbf{v} \cdot \mathbf{n} \equiv v_r \tag{2.26}$$

evaluated at the drop surface, where $\mathbf{v}$ is the drop center velocity in the particle-fixed coordinates. Substituting the Cartesian components of the normal vector over the spherical interfaces in the kinematic boundary condition (2.26),

$$\mathbf{n} = [n_x, n_\sigma \cos \varphi, n_\sigma \sin \varphi], \tag{2.27}$$

we find

$$\mathbf{u} = (v_x n_x + v_y n_\sigma \cos \varphi + v_z n_\sigma \sin \varphi) \, \mathbf{e}_r + u_\theta \, \mathbf{e}_\theta + u_\varphi \, \mathbf{e}_\varphi, \tag{2.28}$$

where u_θ is the velocity component in the direction of the azimuthal unit vector, $\mathbf{e}_\theta$, and u_φ is the velocity component in the direction of the meridional unit vector, $\mathbf{e}_\varphi$. In terms of cylindrical polar unit vectors,

$$\mathbf{u} = (v_x n_x + v_y n_\sigma \cos \varphi + v_z n_\sigma \sin \varphi) \, (n_x \mathbf{e}_x + n_\sigma \mathbf{e}_\sigma) + u_\theta \, (-n_\sigma \mathbf{e}_x + n_x \mathbf{e}_\sigma) + u_\varphi \, \mathbf{e}_\varphi, \tag{2.29}$$

where $\mathbf{e}_\sigma$ is the unit vector normal to the x-axis. Rearranging, we derive the interfacial conditions

$$\begin{aligned} u_x &= n_x \, (v_x n_x + v_y n_\sigma \cos \varphi + v_z n_\sigma \sin \varphi) - u_\theta \, n_\sigma, \\ u_\sigma &= n_\sigma \, (v_x n_x + v_y n_\sigma \cos \varphi + v_z n_\sigma \sin \varphi) + u_\theta \, n_x, \end{aligned} \tag{2.30}$$

involving the drop center velocity and the azimuthal component of the fluid velocity, u_θ. A continuity condition is imposed on the meridional component of the interfacial velocity, u_φ.

The jump in the traction across each interface, $\mathbf{f} \equiv \boldsymbol{\sigma} \cdot \mathbf{n}$, can be resolved into its spherical polar components, $\Delta \mathbf{f} = \Delta f_n \, \mathbf{n} + \Delta f_\theta \, \mathbf{e}_\theta + \Delta f_\varphi \, \mathbf{e}_\varphi$, where $\boldsymbol{\sigma}$ is the stress tensor in the particle coordinates, Δf_θ is the component in

the direction of the unit vector, $\mathbf{e}_\theta$, and Δf_φ is the component in the direction of the unit vector $\mathbf{e}_\varphi$. In cylindrical polar coordinates,

$$\Delta \mathbf{f} = \Delta f_n \, (n_x \mathbf{e}_x + n_\sigma \mathbf{e}_\sigma) + \Delta f_\theta \, (-n_\sigma \mathbf{e}_x + n_x \mathbf{e}_\sigma) + \Delta f_\varphi \, \mathbf{e}_\varphi. \tag{2.31}$$

The equations of (2.16) provide us with expressions for the normal and tangential components of the jump in the disturbance interfacial traction,

$$\Delta f_n^D \equiv \Delta \mathbf{f}^D \cdot \mathbf{n} = 2\mu_1 U \kappa_m^{(1)}, \quad \Delta f_\theta^D = 0, \quad \Delta f_\varphi^D = 0. \tag{2.32}$$

In summary, the interfacial distributions of u_θ, u_φ, and Δf_n^D must be found as part of the solution, and the drop center velocity must be computed to ensure a specified particle force.

The motion of the center of each drop in the laboratory frame, $\mathbf{X}_c$, is governed by the ordinary differential equation

$$\frac{d\mathbf{X}_c}{dt} = \mathbf{A} \cdot \mathbf{v}. \tag{2.33}$$

If the drop center velocity is available, this equation can be integrated in time using a standard numerical method.

2.3 Fourier expansions

A key observation is that the boundaries of the flow, but not the flow itself, are axially symmetric with respect to the x-axis. This geometrical property allows us to simplify the problem by expressing the cylindrical or spherical polar components of all variables of interest in Fourier series with respect to the meridional angle, φ.

We begin by expressing the cylindrical polar components of the incident linear flow as a five-term Fourier series,

$$\begin{bmatrix} u_x^\infty \\ u_\sigma^\infty \\ u_\varphi^\infty \end{bmatrix} = \begin{bmatrix} v_x^\infty + M_{11} x \\ \frac{1}{2}(M_{22} + M_{33})\sigma \\ \frac{1}{2}(M_{23} - M_{32})\sigma \end{bmatrix} + \begin{bmatrix} M_{21}\sigma \\ v_y^\infty + M_{12} x \\ v_z^\infty + M_{13} x \end{bmatrix} \cos\varphi + \begin{bmatrix} M_{31}\sigma \\ v_z^\infty + M_{13} x \\ -v_y^\infty - M_{12} x \end{bmatrix} \sin\varphi$$

$$+ \frac{1}{2} \begin{bmatrix} 0 \\ (M_{22} - M_{33})\sigma \\ (M_{23} + M_{32})\sigma \end{bmatrix} \cos 2\varphi + \frac{1}{2} \begin{bmatrix} 0 \\ (M_{23} + M_{32})\sigma \\ (-M_{22} + M_{33})\sigma \end{bmatrix} \sin 2\varphi. \tag{2.34}$$

Motivated by these forms, we express the cylindrical or spherical polar components of the velocity field as truncated Fourier series,

$$u_\alpha(x, \sigma, \varphi) = \mathcal{U}_{\alpha 0}(x, \sigma) + \sum_{m=1}^{2} [\mathcal{U}_{\alpha m}^c(x, \sigma) \cos(m\varphi) + \mathcal{U}_{\alpha m}^s(x, \sigma) \sin(m\varphi)], \tag{2.35}$$

where Greek indices take the values $x, \sigma, \varphi, \theta, r$, and $\mathcal{U}_{\alpha 0}$, $\mathcal{U}_{\alpha m}^c$ and $\mathcal{U}_{\alpha m}^s$ are Fourier coefficients.

Comparing the interfacial conditions (2.30) with (2.35), we derive boundary conditions for the constant velocity Fourier coefficients,

$$\mathcal{U}_{x0} = n_x^2 \, v_x - n_\sigma \, \mathcal{U}_{\theta 0}, \quad \mathcal{U}_{\sigma 0} = n_x (n_\sigma \, v_x + \mathcal{U}_{\theta 0}), \tag{2.36}$$

first-order velocity Fourier coefficients,

$$\mathcal{U}_{x1}^c = n_\sigma (n_x v_y - \mathcal{U}_{\theta 1}^c), \quad \mathcal{U}_{\sigma 1}^c = n_\sigma^2 v_y + n_x \, \mathcal{U}_{\theta 1}^c,$$
$$\mathcal{U}_{x1}^s = n_\sigma (n_x v_z - \mathcal{U}_{\theta 1}^s), \quad \mathcal{U}_{\sigma 1}^s = n_\sigma^2 v_z + n_x \, \mathcal{U}_{\theta 1}^s, \tag{2.37}$$

and second-order velocity Fourier coefficients,

$$\mathcal{U}_{x2}^c = -\mathcal{U}_{\theta 2}^c \, n_\sigma, \quad \mathcal{U}_{\sigma 2}^c = \mathcal{U}_{\theta 2}^c \, n_x, \quad \mathcal{U}_{x2}^s = -\mathcal{U}_{\theta 2}^s \, n_\sigma, \quad \mathcal{U}_{\sigma 2}^s = \mathcal{U}_{\theta 2}^s \, n_x. \tag{2.38}$$

These expressions allow us to compute the coefficients $\mathcal{U}_{xm}$ and $\mathcal{U}_{\sigma m}$ in terms of the drop center velocity, $\mathbf{v}$, and azimuthal coefficients, $\mathcal{U}_{\theta m}$. Boundary conditions for the meridional coefficients $\mathcal{U}_{\varphi m}$ are not available.

Working in a similar fashion, we express the cylindrical polar components of the jump in the disturbance interfacial traction in a truncated Fourier series,

$$\Delta f_\alpha^D(x, \varphi) = \Delta\mathcal{F}_{\alpha 0}(x, \sigma) + \sum_{m=1}^{2} [\Delta\mathcal{F}_{\alpha m}^c(x)\cos(m\varphi) + \Delta\mathcal{F}_{\alpha m}^s(x)\sin(m\varphi)], \tag{2.39}$$

where $\Delta\mathcal{F}_{\alpha 0}$, $\Delta\mathcal{F}_{\alpha m}^c$, and $\Delta\mathcal{F}_{\alpha m}^s$ are corresponding Fourier coefficients. The Cartesian components of the force exerted on each drop surface, $\mathcal{D}$, are given by

$$F_x = \iint_{\mathcal{D}} \Delta f_x^D \, dS = 2\pi \int_C \Delta\mathcal{F}_{x0}\, \sigma \, dl,$$

$$F_y = \iint_{\mathcal{D}} (\Delta f_\sigma^D \cos\varphi - \Delta f_\varphi^D \sin\varphi) \, dS = \pi \int_C (\Delta\mathcal{F}_{\sigma 1}^c - \Delta\mathcal{F}_{\varphi 1}^s)\, \sigma \, dl, \tag{2.40}$$

$$F_z = \iint_{\mathcal{D}} (\Delta f_\sigma^D \sin\varphi + \Delta f_\varphi^D \cos\varphi) \, dS = \pi \int_C (\Delta\mathcal{F}_{\sigma 1}^s + \Delta\mathcal{F}_{\varphi 1}^c)\, \sigma \, dl,$$

where C is the contour of the drop surface in a meridional plane, and l is the arc length along C. It is remarkable that the force depends only on the zeroth and first Fourier coefficients and is independent of the second Fourier coefficients.

The interfacial boundary conditions require $\Delta\mathcal{F}_{\theta m} = 0$ and $\Delta\mathcal{F}_{\varphi m} = 0$, yielding the simplified expressions

$$F_x = 2\pi \int_C \Delta\mathcal{F}_{x0}\, \sigma \, dl, \quad F_y = \pi \int_C \Delta\mathcal{F}_{\sigma 1}^c \, \sigma \, dl, \quad F_z = \pi \int_C \Delta\mathcal{F}_{\sigma 1}^s \, \sigma \, dl. \tag{2.41}$$

Over the drop surface, the cylindrical polar components are related to the radial spherical polar component of the jump in the interfacial traction by

$$\Delta\mathcal{F}_{xm} = n_x \Delta\mathcal{F}_{rm}, \quad \Delta\mathcal{F}_{\sigma m} = n_\sigma \Delta\mathcal{F}_{rm}, \quad \Delta\mathcal{F}_{\varphi m} = 0, \tag{2.42}$$

for $m = 0, 1, 2$. Thus, the Cartesian components of the force exerted on each drop are given by

$$F_x = 2\pi \int_C \Delta\mathcal{F}_{r0}\, n_x \, \sigma \, dl, \quad F_y = \pi \int_C \Delta\mathcal{F}_{r1}^c\, n_\sigma \, \sigma \, dl, \quad F_z = \pi \int_C \Delta\mathcal{F}_{r1}^s\, n_\sigma \, \sigma \, dl. \tag{2.43}$$

3 Boundary-integral formulation

The governing equations will be solved in the particle-fixed coordinates using the boundary-integral formulation for Stokes flow. As a preliminary, we introduce the single- and double-layer potential of Stokes flow defined over a generic surface, $\mathcal{R}$,

$$\mathcal{S}_j(\mathbf{x}_0, \mathbf{f}; \mathcal{R}) \equiv \iint_{\mathcal{R}} f_i(\mathbf{x})\, G_{ij}(\mathbf{x}, \mathbf{x}_0) \, dS(\mathbf{x}),$$

$$\mathcal{D}_j(\mathbf{x}_0, \mathbf{u}; \mathcal{R}) \equiv \iint_{\mathcal{R}} u_i(\mathbf{x})\, T_{ijk}(\mathbf{x}, \mathbf{x}_0)\, n_k(\mathbf{x}) \, dS(\mathbf{x}), \tag{3.1}$$

where

$$G_{ij}(\mathbf{x}, \mathbf{x}_0) = \frac{\delta_{ij}}{r} + \frac{\hat{x}_i \hat{x}_j}{r^3}, \quad T_{ijk}(\mathbf{x}, \mathbf{x}_0) = -6\,\frac{\hat{x}_i \hat{x}_j \hat{x}_k}{r^5}, \tag{3.2}$$

are the free-space Green's function and associated stress tensors, $\hat{\mathbf{x}} = \mathbf{x} - \mathbf{x}_0$, $r = |\hat{\mathbf{x}}|$, and δ_{ij} is Kronecker's delta; e.g., [15, Chap. 3].

The disturbance velocity at a point $\mathbf{x}_0$ that lies in the ambient fluid can be expressed in terms of integrals over the drop interfaces, $\mathcal{D}_1$ and $\mathcal{D}_2$,

$$8\pi\mu_1\mathbf{u}^D(\mathbf{x}_0) = -\boldsymbol{\mathcal{S}}(\mathbf{x}_0, \mathbf{f}^{D_1}; \mathcal{D}_1, \mathcal{D}_2) + \mu_1\,\boldsymbol{\mathcal{D}}(\mathbf{x}_0, \mathbf{u}^{D_1}; \mathcal{D}_1, \mathcal{D}_2), \tag{3.3}$$

where the superscript D_1 denotes the disturbance flow on the side of the ambient fluid. The reciprocal theorem for the flow in the interior of each drop applied at the same point $\mathbf{x}_0$ outside the drops requires

$$-\mathcal{S}(\mathbf{x}_0, \mathbf{f}^{D_2}; \mathcal{D}_1) + \mu_2\mathcal{D}(\mathbf{x}_0, \mathbf{u}^{D_2}; \mathcal{D}_1) = \mathbf{0}, \quad -\mathcal{S}(\mathbf{x}_0, \mathbf{f}^{D_3}; \mathcal{D}_2) + \mu_3\mathcal{D}(\mathbf{x}_0, \mathbf{u}^{D_3}; \mathcal{D}_2) = \mathbf{0}, \tag{3.4}$$

where the superscripts D_2 and D_3 denote the disturbance flow on the side of the drops. Combining these equations to formulate the jump in traction across the interfaces, we find

$$8\pi\mu_1\,\mathbf{u}^D(\mathbf{x}_0) = -\mathcal{S}(\mathbf{x}_0, \Delta\mathbf{f}^D; \mathcal{D}_1, \mathcal{D}_2) + \mathcal{D}(\mathbf{x}_0, \mu_1\mathbf{u}^{D_1} - \mu_2\mathbf{u}^{D_2}; \mathcal{D}_1) + \mathcal{D}(\mathbf{x}_0, \mu_1\mathbf{u}^{D_1} - \mu_3\mathbf{u}^{D_3}; \mathcal{D}_2). \tag{3.5}$$

Continuity of velocity across the first drop interface requires

$$\mathbf{u}^{B_1} + \mathbf{u}^{D_1} = \mathbf{u}^{B_2} + \mathbf{u}^{D_2} = \frac{\mu_1}{\mu_2}\mathbf{u}_1^{B_1} + \mathbf{u}^{D_2}, \tag{3.6}$$

and thus

$$\mu_2\,\mathbf{u}^{D_2} = (\mu_2 - \mu_1)\,\mathbf{u}^{B_1} + \mu_2\,\mathbf{u}^{D_1} = (\mu_2 - \mu_1)\,\mathbf{u} + \mu_1\,\mathbf{u}^{D_1}. \tag{3.7}$$

Substituting this expression and a similar expression for the second interface in the second and third terms on the right-hand side of (3.5) and rearranging, we find

$$\mathbf{u}(\mathbf{x}_0) = \mathbf{u}^{B,1}(\mathbf{x}_0) - \frac{1}{8\pi\mu_1}\,\mathcal{S}(\mathbf{x}_0, \Delta\mathbf{f}^D; \mathcal{D}_1, \mathcal{D}_2) + \frac{\mu_1 - \mu_2}{8\pi\mu_1}\,\mathcal{D}(\mathbf{x}_0, \mathbf{u}; \mathcal{D}_1) + \frac{\mu_1 - \mu_3}{8\pi\mu_1}\,\mathcal{D}(\mathbf{x}_0, \mathbf{u}; \mathcal{D}_2). \tag{3.8}$$

Now taking the limit as the field point $\mathbf{x}_0$ approaches the surface of the first drop and rearranging, we derive the integral equation

$$\mathcal{S}(\mathbf{x}_0, \Delta\mathbf{f}^D; \mathcal{D}_1; \mathcal{D}_2) - (\mu_1 - \mu_2)\,\mathcal{D}^{\text{PV}}(\mathbf{x}_0, \mathbf{u}; \mathcal{D}_1) - (\mu_1 - \mu_3)\,\mathcal{D}(\mathbf{x}_0, \mathbf{u}; \mathcal{D}_2)$$
$$+ 4\pi(\mu_1 + \mu_2)\,\mathbf{u}(\mathbf{x}_0) = 8\pi\mu_1\mathbf{u}^\infty, \tag{3.9}$$

where PV denotes the principal value of the double-layer integral. Taking also the limit as the field point $\mathbf{x}_0$ approaches the surface of the second drop and rearranging, we derive the integral equation

$$\mathcal{S}(\mathbf{x}_0, \Delta\mathbf{f}^D; \mathcal{D}_1, \mathcal{D}_2) - (\mu_1 - \mu_2)\,\mathcal{D}(\mathbf{x}_0, \mathbf{u}; \mathcal{D}_1) - (\mu_1 - \mu_3)\,\mathcal{D}^{\text{PV}}(\mathbf{x}_0, \mathbf{u}; \mathcal{D}_2)$$
$$+ 4\pi(\mu_1 + \mu_3)\,\mathbf{u}(\mathbf{x}_0) = 8\pi\mu_1\mathbf{u}^\infty. \tag{3.10}$$

These integral equations are accompanied by the condition of a specified force on each spherical drop.

3.1 Fourier expansion of the single-layer potential

The Cartesian components of the single-layer potential over an axisymmetric surface, $\mathcal{R}$, take the form

$$\mathcal{S}_j(\mathbf{x}_0, \mathbf{f}; \mathcal{R}) = \iint\limits_{\mathcal{R}} \left[\frac{f_j}{(\hat{x}^2 + \hat{y}^2 + \hat{z}^2)^{1/2}} + \frac{f_x\,\hat{x} + f_y\,\hat{y} + f_z\,\hat{z}}{(\hat{x}^2 + \hat{y}^2 + \hat{z}^2)^{3/2}}\,(\mathbf{x} - \mathbf{x}_0)_j \right]\,\mathrm{d}S(\mathbf{x})$$

$$= \iint\limits_{\mathcal{R}} \left[\frac{f_j}{(\hat{x}^2 + \sigma^2 + \sigma_0^2 - 2\sigma\sigma_0\cos\hat{\varphi})^{1/2}} \right.$$

$$\left. + \frac{f_x\,\hat{x} + f_\sigma\,(\sigma - \sigma_0\cos\hat{\varphi}) + f_\varphi\,\sigma_0\,\sin\hat{\varphi}}{(\hat{x}^2 + \sigma^2 + \sigma_0^2 - 2\sigma\sigma_0\cos\hat{\varphi})^{3/2}}\,(\mathbf{x} - \mathbf{x}_0)_j \right]\,\mathrm{d}S(\mathbf{x}), \tag{3.11}$$

where $\hat{\mathbf{x}} = \mathbf{x} - \mathbf{x}_0$. The associated cylindrical polar components are

$$
\begin{bmatrix} \mathcal{S}_x \\ \mathcal{S}_\sigma \\ \mathcal{S}_\varphi \end{bmatrix} (\mathbf{x}_0, \mathbf{f}; \mathcal{R}) = \iint\limits_P \frac{1}{(\hat{x}^2 + \sigma^2 + \sigma_0^2 - 2\sigma\sigma_0 \cos\hat{\varphi})^{1/2}} \begin{bmatrix} f_x \\ f_\sigma \cos\hat{\varphi} - f_\varphi \sin\hat{\varphi} \\ f_\sigma \sin\hat{\varphi} + f_\varphi \cos\hat{\varphi} \end{bmatrix}
$$

$$
+ \frac{f_x \hat{x} + f_\sigma (\sigma - \sigma_0 \cos\hat{\varphi}) + f_\varphi \sigma_0 \sin\hat{\varphi}}{(\hat{x}^2 + \sigma^2 + \sigma_0^2 - 2\sigma\sigma_0 \cos\hat{\varphi})^{3/2}} \times \begin{bmatrix} \hat{x} \\ \sigma \cos\hat{\varphi} - \sigma_0 \\ \sigma \sin\hat{\varphi} \end{bmatrix} \, \mathrm{d}S(\mathbf{x}). \tag{3.12}
$$

Substituting the Fourier expansion (2.39), performing the integration with respect to the meridional angle, φ, and simplifying, we find

$$
\mathcal{S}_\alpha(\mathbf{x}_0) = \sum_{m=0}^{2} \int\limits_C \begin{bmatrix} \mathcal{P}_{xxm} \cos(m\varphi_0) & \mathcal{P}_{x\sigma m} \cos(m\varphi_0) & \mathcal{P}_{x\varphi m} \sin(m\varphi_0) \\ \mathcal{P}_{\sigma xm} \cos(m\varphi_0) & \mathcal{P}_{\sigma\sigma m} \cos(m\varphi_0) & \mathcal{P}_{\sigma\varphi m} \sin(m\varphi_0) \\ \mathcal{P}_{\varphi xm} \sin(m\varphi_0) & \mathcal{P}_{\varphi\sigma m} \sin(m\varphi_0) & \mathcal{P}_{\varphi\varphi m} \cos(m\varphi_0) \end{bmatrix} \cdot \begin{bmatrix} \mathcal{F}_{xm}^c \\ \mathcal{F}_{\sigma m}^c \\ \mathcal{F}_{\varphi m}^c \end{bmatrix}
$$

$$
+ \begin{bmatrix} \mathcal{P}_{xxm} \sin(m\varphi_0) & \mathcal{P}_{x\sigma m} \sin(m\varphi_0) & -\mathcal{P}_{x\varphi m} \cos(m\varphi_0) \\ \mathcal{P}_{\sigma xm} \sin(m\varphi_0) & \mathcal{P}_{\sigma\sigma m} \sin(m\varphi_0) & -\mathcal{P}_{\sigma\varphi m} \cos(m\varphi_0) \\ -\mathcal{P}_{\varphi xm} \cos(m\varphi_0) & -\mathcal{P}_{\varphi\sigma m} \cos(m\varphi_0) & \mathcal{P}_{\varphi\varphi m} \sin(m\varphi_0) \end{bmatrix} \cdot \begin{bmatrix} \mathcal{F}_{xm}^s \\ \mathcal{F}_{\sigma m}^s \\ \mathcal{F}_{\varphi m}^s \end{bmatrix} \, \mathrm{d}l(\mathbf{x}), \tag{3.13}
$$

where C is the trace of $\mathcal{R}$ is a meridional plane. The dimensionless single-layer kernels, $\mathcal{P}_{\alpha\beta\gamma}$, are given in Appendix A.

3.2 Fourier expansion of the double-layer potential

The Cartesian components of the double-layer potential over an axisymmetric surface, $\mathcal{R}$, take the form

$$
\mathcal{D}_j(\mathbf{x}_0, \mathbf{u}, P) = -6 \iint\limits_P \frac{u_x \hat{x} + u_y \hat{y} + u_z \hat{z}}{(\hat{x}^2 + \hat{y}^2 + \hat{z}^2)^{5/2}} (\mathbf{x} - \mathbf{x}_0)_j (\mathbf{x} - \mathbf{x}_0) \cdot \mathbf{n}(\mathbf{x}) \, \mathrm{d}S(\mathbf{x})
$$

$$
= -6 \iint\limits_P \frac{u_x \hat{x} + u_\sigma (\sigma - \sigma_0 \cos\hat{\varphi}) + u_\varphi \sigma_0 \sin\hat{\varphi}}{(\hat{x}^2 + \sigma^2 + \sigma_0^2 - 2\sigma\sigma_0 \cos\hat{\varphi})^{5/2}} (\mathbf{x} - \mathbf{x}_0)_j \, \mathcal{G} \, \mathrm{d}S(\mathbf{x}), \tag{3.14}
$$

where $\mathcal{G} = n_x \hat{x} + n_\sigma (\sigma - \sigma_0 \cos\hat{\varphi})$. The associated cylindrical polar components are

$$
\begin{bmatrix} \mathcal{D}_x \\ \mathcal{D}_\sigma \\ \mathcal{D}_\varphi \end{bmatrix} (\mathbf{x}_0, \mathbf{u}; \mathcal{R}) = -\frac{6}{a} \iint\limits_P \frac{u_x \hat{x} + u_\sigma (\sigma - \sigma_0 \cos\hat{\varphi}) + u_\varphi \sigma_0 \sin\hat{\varphi}}{(\hat{x}^2 + \sigma^2 + \sigma_0^2 - 2\sigma\sigma_0 \cos\hat{\varphi})^{5/2}} \begin{bmatrix} \hat{x} \\ \sigma \cos\hat{\varphi} - \sigma_0 \\ \sigma \sin\hat{\varphi} \end{bmatrix} \mathcal{G} \, \mathrm{d}S(\mathbf{x}). \tag{3.15}
$$

Substituting (2.35), performing the integration with respect to the meridional angle, φ and simplifying, we find

$$
\mathcal{D}_\alpha(\mathbf{x}_0) = \sum_{m=0}^{2} \int\limits_C \begin{bmatrix} \mathcal{R}_{xxm} \cos(m\varphi_0) & \mathcal{R}_{x\sigma m} \cos(m\varphi_0) & \mathcal{R}_{x\varphi m} \sin(m\varphi_0) \\ \mathcal{R}_{\sigma xm} \cos(m\varphi_0) & \mathcal{R}_{\sigma\sigma m} \cos(m\varphi_0) & \mathcal{R}_{\sigma\varphi m} \sin(m\varphi_0) \\ \mathcal{R}_{\varphi xm} \sin(m\varphi_0) & \mathcal{R}_{\varphi\sigma m} \sin(m\varphi_0) & \mathcal{R}_{\varphi\varphi m} \cos(m\varphi_0) \end{bmatrix} \cdot \begin{bmatrix} \mathcal{U}_{xm}^c \\ \mathcal{U}_{\sigma m}^c \\ \mathcal{U}_{\varphi m}^c \end{bmatrix}
$$

$$
+ \begin{bmatrix} \mathcal{R}_{xxm} \sin(m\varphi_0) & \mathcal{R}_{x\sigma m} \sin(m\varphi_0) & -\mathcal{R}_{x\varphi m} \cos(m\varphi_0) \\ \mathcal{R}_{\sigma xm} \sin(m\varphi_0) & \mathcal{R}_{\sigma\sigma m} \sin(m\varphi_0) & -\mathcal{R}_{\sigma\varphi m} \cos(m\varphi_0) \\ -\mathcal{R}_{\varphi xm} \cos(m\varphi_0) & -\mathcal{R}_{\varphi\sigma m} \cos(m\varphi_0) & \mathcal{R}_{\varphi\varphi m} \sin(m\varphi_0) \end{bmatrix} \cdot \begin{bmatrix} \mathcal{U}_{xm}^s \\ \mathcal{U}_{\sigma m}^s \\ \mathcal{U}_{\varphi m}^s \end{bmatrix} \, \mathrm{d}l(\mathbf{x}), \tag{3.16}
$$

The double-layer kernels, $\mathcal{R}_{\alpha\beta\gamma}$, are given in Appendix B.

3.3 One-dimensional integral equations

Substituting the Fourier expansions of the hydrodynamic potentials and other flow variables in the integral equations (3.9) and (3.10) and collecting corresponding Fourier coefficients, we derive three decoupled systems of

integral equations for $m = 0, 1, 2$ that can be solved separately and in isolation. In practice, depending on the flow configuration and specific objectives of the computation, only a subset of these equations may need to be solved.

3.4 Integral equations for the zeroth-order Fourier coefficients

For $m = 0$, we derive the integral equation

$$
\int_{C_1,C_2} \mathcal{P}_{\alpha\beta 0} \, \Delta\mathcal{F}_{\beta 0} \, \mathrm{d}l - (\mu_1 - \mu_2) \int_{C_1}^{\mathrm{PV}} \mathcal{R}_{\alpha\beta 0} \, \mathcal{U}_{\beta 0} \, \mathrm{d}l
$$

$$
- (\mu_1 - \mu_3) \int_{C_2} \mathcal{R}_{\alpha\beta 0} \, \mathcal{U}_{\beta 0} \, \mathrm{d}l + 4\pi(\mu_1 + \mu_2) \mathcal{U}_{\alpha 0} = 8\pi\mu_1 \mathcal{U}_{\alpha 0}^{\infty} \tag{3.17}
$$

for a point that lies at the first drop contour, and the integral equation

$$
\int_{C_1,C_2} \mathcal{P}_{\alpha\beta 0} \, \Delta\mathcal{F}_{\beta 0} \, \mathrm{d}l - (\mu_1 - \mu_2) \int_{C_1} \mathcal{R}_{\alpha\beta 0} \, \mathcal{U}_{\beta 0} \, \mathrm{d}l
$$

$$
- (\mu_1 - \mu_3) \int_{C_2}^{\mathrm{PV}} \mathcal{R}_{\alpha\beta 0} \, \mathcal{U}_{\beta 0} \, \mathrm{d}l + 4\pi(\mu_1 + \mu_3) \mathcal{U}_{\alpha 0} = 8\pi\mu_1 \mathcal{U}_{\alpha 0}^{\infty} \tag{3.18}
$$

for a point that lies at the second drop contour, where

$$
\mathcal{U}_{x0}^{\infty} = v_x^{\infty} + M_{11} x, \quad \mathcal{U}_{\sigma 0}^{\infty} = \frac{1}{2} \left(M_{22} + M_{33} \right) \sigma, \quad \mathcal{U}_{\varphi 0}^{\infty} = \frac{1}{2} \left(M_{23} - M_{32} \right) \sigma, \tag{3.19}
$$

Inspecting the kernels, we find that this system can be further decomposed into a first subsystem of two integral equations for the axial (x) and radial (σ) components of the traction, and a second subsystem of one integral equation for the meridional (φ) component of the traction. Physically, the first subsystem describes axisymmetric uniaxial, biaxial, or two-dimensional straining flow, and the second subsystem describes a contrived swirling flow expressing rigid-body rotation.

Implementing the interfacial conditions (2.36) and (2.42) in the first subsystem, we derive integral equations for $\Delta\mathcal{F}_{r0}$ and $\mathcal{U}_{\theta 0}$. For a point that lies at the contour of the first drop, we find

$$
\int_{C_1,C_2} (\mathcal{P}_{\alpha x0} \, n_x + \mathcal{P}_{\alpha\sigma 0} \, n_\sigma) \, \Delta\mathcal{F}_{r0} \, \mathrm{d}l + (\mu_1 - \mu_2) \int_{C_1}^{\mathrm{PV}} (\mathcal{R}_{\alpha x0} \, n_\sigma - \mathcal{R}_{\alpha\sigma 0} \, n_x) \mathcal{U}_{\theta 0} \, \mathrm{d}l
$$

$$
+ (\mu_1 - \mu_3) \int_{C_2} (\mathcal{R}_{\alpha x0} \, n_\sigma - \mathcal{R}_{\alpha\sigma 0} \, n_x) \mathcal{U}_{\theta 0} \, \mathrm{d}l - (\mu_1 - \mu_2) v_x^{(1)} \int_{C_1}^{\mathrm{PV}} (\mathcal{R}_{\alpha x0} \, n_x + \mathcal{R}_{\alpha\sigma 0} \, n_\sigma) \, n_x \, \mathrm{d}l
$$

$$
- (\mu_1 - \mu_3) v_x^{(2)} \int_{C_2} (\mathcal{R}_{\alpha x0} \, n_x + \mathcal{R}_{\alpha\sigma 0} \, n_\sigma) \, n_x \, \mathrm{d}l
$$

$$
+ 4\pi(\mu_1 + \mu_2) \left[\delta_{\alpha x} (n_x^2 v_x^{(1)} - \mathcal{U}_{\theta 0} \, n_\sigma) + \delta_{\alpha\sigma} n_x (n_\sigma v_x^{(1)} + \mathcal{U}_{\theta 0}) \right] = 8\pi\mu_1 \mathcal{U}_{\alpha 0}^{\infty}, \tag{3.20}
$$

where $\alpha = x, \sigma$. For a point that lies at the contour of the second drop, we find

$$
\int_{C_1,C_2} (\mathcal{P}_{\alpha x0} \, n_x + \mathcal{P}_{\alpha\sigma 0} \, n_\sigma) \, \Delta\mathcal{F}_{r0} \, \mathrm{d}l + (\mu_1 - \mu_2) \int_{C_1} (\mathcal{R}_{\alpha x0} \, n_\sigma - \mathcal{R}_{\alpha\sigma 0} \, n_x) \mathcal{U}_{\theta 0} \, \mathrm{d}l
$$

$$+(\mu_1 - \mu_3) \int\limits_{C_2}^{\mathrm{PV}} (\mathcal{R}_{\alpha x 0}\, n_\sigma - \mathcal{R}_{\alpha \sigma 0}\, n_x)\, \mathcal{U}_{\theta 0}\, \mathrm{d}l - (\mu_1 - \mu_2)\, v_x^{(1)} \int\limits_{C_1} (\mathcal{R}_{\alpha x 0}\, n_x + \mathcal{R}_{\alpha \sigma 0}\, n_\sigma)\, n_x\, \mathrm{d}l$$

$$-(\mu_1 - \mu_3) v_x^{(2)} \int\limits_{C_2}^{\mathrm{PV}} (\mathcal{R}_{\alpha x 0}\, n_x + \mathcal{R}_{\alpha \sigma 0}\, n_\sigma)\, n_x\, \mathrm{d}l + 4\pi\, (\mu_1 + \mu_2)\, [\, \delta_{\alpha x}\, (n_x^2 v_x^{(2)} - \mathcal{U}_{\theta 0}\, n_\sigma)$$

$$+\delta_{\alpha \sigma}\, n_x\, (n_\sigma v_x^{(2)} + \mathcal{U}_{\theta 0})] = 8\pi\, \mu_1\, \mathcal{U}_{\alpha 0}^\infty, \tag{3.21}$$

where $\alpha = x, \sigma$. The x components of the drop translational velocities are computed to ensure that the x component of the force exerted on each drop has a specified value, according to the first equation in (2.43).

The solution of the integral equations for the normal jump in the traction, $\Delta \mathcal{F}_{r0}$, is not unique. Any solution can be uniformly shifted by an arbitrary constant to yield another acceptable solution. In computing the deformed drop shape from the curvature, the value of this constant is fixed so that the volume of the deformed drop is preserved to leading order with respect to the capillary number.

3.5 Integral equations for the first- and second-order Fourier coefficients

Substituting the Fourier expansions for $m = 1, 2$ in the integral equations (3.9) and (3.10), and enforcing the interfacial condition for the disturbance interfacial traction, we derive a further system of integral equations. For a point that lies at the first drop contour, the integral equations corresponding to the cosine Fourier coefficients yield

$$\int\limits_{C_1, C_2} (\mathcal{P}_{\alpha x m} n_x + \mathcal{P}_{\alpha \sigma m} n_\sigma)\, \Delta \mathcal{F}_{rm}^c\, \mathrm{d}l - (\mu_1 - \mu_2) \int\limits_{C_1}^{\mathrm{PV}} (\mathcal{R}_{\alpha \beta m}\, \mathcal{U}_{\beta m}^c - \mathcal{R}_{\alpha \varphi m}\, \mathcal{U}_{\varphi m}^s)\, \mathrm{d}l$$

$$-(\mu_1 - \mu_3) \int\limits_{C_2} (\mathcal{R}_{\alpha \beta m}\, \mathcal{U}_{\beta m}^c - \mathcal{R}_{\alpha \varphi m}\, \mathcal{U}_{\varphi m}^s)\, \mathrm{d}l + 4\pi\, (\mu_1 + \mu_2)\, \mathcal{U}_{\alpha m}^c = 8\pi\, \mu_1\, \mathcal{U}_{\alpha m}^{c\infty}, \tag{3.22}$$

and

$$\int\limits_{C_1, C_2} (\mathcal{P}_{\varphi x m} n_x + \mathcal{P}_{\varphi x m} n_\sigma)\, \Delta \mathcal{F}_{rm}^c\, \mathrm{d}l - (\mu_1 - \mu_2) \int\limits_{C_1}^{\mathrm{PV}} (\mathcal{R}_{\varphi \beta m}\, \mathcal{U}_{\beta m}^c + \mathcal{R}_{\varphi \varphi m}\, \mathcal{U}_{\varphi m}^s)\, \mathrm{d}l$$

$$-(\mu_1 - \mu_3) \int\limits_{C_2} (\mathcal{R}_{\varphi \beta m}\, \mathcal{U}_{\beta m}^c + \mathcal{R}_{\varphi \varphi m}\, \mathcal{U}_{\varphi m}^s)\, \mathrm{d}l + 4\pi\, (\mu_1 + \mu_2)\, \mathcal{U}_{\varphi m}^s = 8\pi\, \mu_1\, \mathcal{U}_{\varphi m}^{s\infty}, \tag{3.23}$$

where $\alpha, \beta = x, \sigma$. The integral equations corresponding to the sine Fourier coefficients yield the corresponding equations

$$\int\limits_{C_1, C_2} (\mathcal{P}_{\alpha x m} n_x + \mathcal{P}_{\alpha \sigma m} n_\sigma)\, \Delta \mathcal{F}_{rm}^s\, \mathrm{d}l - (\mu_1 - \mu_2) \int\limits_{C_1}^{\mathrm{PV}} (\mathcal{R}_{\alpha \beta m}\, \mathcal{U}_{\beta m}^s + \mathcal{R}_{\alpha \varphi m}\, \mathcal{U}_{\varphi m}^c)\, \mathrm{d}l$$

$$-(\mu_1 - \mu_3) \int\limits_{C_2} (\mathcal{R}_{\alpha \beta m}\, \mathcal{U}_{\beta m}^s + \mathcal{R}_{\alpha \varphi m}\, \mathcal{U}_{\varphi m}^c)\, \mathrm{d}l + 4\pi\, (\mu_1 + \mu_2)\, \mathcal{U}_{\alpha m}^s = 8\pi\, \mu_1\, \mathcal{U}_{\alpha m}^{s\infty}, \tag{3.24}$$

and

$$\int\limits_{C_1, C_2} (\mathcal{P}_{\varphi x m} n_x + \mathcal{P}_{\varphi x m} n_\sigma)\, \Delta \mathcal{F}_{rm}^s\, \mathrm{d}l - (\mu_1 - \mu_2) \int\limits_{C_1}^{\mathrm{PV}} (\mathcal{R}_{\varphi \beta m}\, \mathcal{U}_{\beta m}^s - \mathcal{R}_{\varphi \varphi m}\, \mathcal{U}_{\varphi m}^c)\, \mathrm{d}l$$

$$-(\mu_1 - \mu_3) \int\limits_{C_2} (\mathcal{R}_{\varphi \beta m}\, \mathcal{U}_{\beta m}^s - \mathcal{R}_{\varphi \varphi m}\, \mathcal{U}_{\varphi m}^c)\, \mathrm{d}l - 4\pi\, (\mu_1 + \mu_2)\, \mathcal{U}_{\varphi m}^c = -8\pi\, \mu_1\, \mathcal{U}_{\varphi m}^{c\infty}, \tag{3.25}$$

where $\alpha, \beta = x, \sigma$. Equations 3.24 and 3.25 arise from 3.22 and 3.23 by replacing the cosine with the sine coefficients, and vice versa, and then flipping the sign of the cosine coefficients. A similar system of equations is written at a point that lies at the second drop contour. The forcing terms on the right-hand sides are given by

$$
\begin{aligned}
\mathcal{U}_{x1}^{c\infty} &= M_{21}\,\sigma, \quad \mathcal{U}_{\sigma1}^{c\infty} = v_y^\infty + M_{12}\,x, \quad \mathcal{U}_{\varphi1}^{c\infty} = v_z^\infty + M_{13}\,x, \\
\mathcal{U}_{x1}^{s\infty} &= M_{31}\,\sigma, \quad \mathcal{U}_{\sigma1}^{s\infty} = v_z^\infty + M_{13}\,x, \quad \mathcal{U}_{\varphi1}^{s\infty} = -v_y^\infty - M_{12}\,x,
\end{aligned}
\tag{3.26}
$$

for the first Fourier coefficients, and

$$
\begin{aligned}
\mathcal{U}_{x2}^{c\infty} &= 0, \quad \mathcal{U}_{\sigma2}^{c\infty} = \frac{1}{2}\,(M_{22} - M_{33})\,\sigma, \quad \mathcal{U}_{\varphi2}^{c\infty} = \frac{1}{2}\,(M_{23} + M_{32})\,\sigma, \\
\mathcal{U}_{x2}^{s\infty} &= 0, \quad \mathcal{U}_{\sigma2}^{s\infty} = \frac{1}{2}\,(M_{23} + M_{32})\,\sigma, \quad \mathcal{U}_{\varphi2}^{c\infty} = -\frac{1}{2}\,(M_{22} - M_{33})\,\sigma,
\end{aligned}
\tag{3.27}
$$

for the second Fourier coefficients. The unknowns are the normal components of the traction jump, $\Delta\mathcal{F}_{rm}$, the tangential azimuthal and meridional velocities, $\mathcal{U}_{\theta m}$ and $\mathcal{U}_{\varphi m}$, and the y- and z-components of the drop center velocities involved in the system for $m = 1$. The drop velocities are computed to ensure that the y- and z-components of the force have specified values according to the second and third equations in (2.43).

3.6 Fluids with equal viscosities

When all fluid viscosities are equal, the integral equations for the cosine and sine coefficients are decoupled. For a point that lies at the first or second drop contour, we find

$$
\int_{C_1,C_2} (\mathcal{P}_{\alpha x m} n_x + \mathcal{P}_{\alpha\sigma m} n_\sigma)\,\Delta\mathcal{F}_{rm}^c\,\mathrm{d}l + 8\pi\mu_1\,\mathcal{U}_{\alpha m}^c = 8\pi\mu_1\,\mathcal{U}_{\alpha m}^{c\infty}
\tag{3.28}
$$

and

$$
\int_{C_1,C_2} (\mathcal{P}_{\alpha x m} n_x + \mathcal{P}_{\alpha\sigma m} n_\sigma)\,\Delta\mathcal{F}_{rm}^s\,\mathrm{d}l + 8\pi\mu_1\,\mathcal{U}_{\alpha m}^s = 8\pi\mu_1\,\mathcal{U}_{\alpha m}^{s\infty},
\tag{3.29}
$$

where $\alpha = x, \sigma$. Implementing the boundary conditions (2.37) for $m = 1$, we find

$$
\begin{aligned}
&\int_{C_1,C_2} (\mathcal{P}_{\alpha x 1} n_x + \mathcal{P}_{\alpha\sigma 1} n_\sigma)\,\Delta\mathcal{F}_{r1}^c\,\mathrm{d}l \\
&\quad + 8\pi\mu_1\,[\delta_{\alpha x} n_\sigma\,(n_x v_y^{(1)} - \mathcal{U}_{\theta1}^c) + \delta_{\alpha\sigma}\,(n_\sigma^2 v_y^{(1)} + n_x\,\mathcal{U}_{\theta1}^c) + (\delta_{\alpha\varphi}\,\mathcal{U}_{\varphi1}^c)] = 8\pi\mu_1\,\mathcal{U}_{\alpha m}^{c\infty}
\end{aligned}
\tag{3.30}
$$

and

$$
\begin{aligned}
&\int_{C_1,C_2} (\mathcal{P}_{\alpha x 1} n_x + \mathcal{P}_{\alpha\sigma 1} n_\sigma)\,\Delta\mathcal{F}_{r1}^s\,\mathrm{d}l \\
&\quad + 8\pi\mu_1\,[\delta_{\alpha x} n_\sigma\,(n_x v_z^{(1)} - \mathcal{U}_{\theta1}^s) + \delta_{\alpha\sigma}\,(n_\sigma^2 v_z^{(1)} + n_x\,\mathcal{U}_{\theta1}^s) + (\delta_{\alpha\varphi}\,\mathcal{U}_{\varphi1}^s)] = 8\pi\mu_1\,\mathcal{U}_{\alpha m}^{s\infty}
\end{aligned}
\tag{3.31}
$$

for a point that lies at the first drop contour. Note that the meridional component of the interfacial velocity, $\mathcal{U}_{\varphi m}$, is not involved. A similar set of equations are written for a point that lies at the second drop contour involving the second drop velocities. Cursory inspection reveals that the integral equations for the first-order cosine coefficients for $\alpha = x$ and σ, also involving the y-components of the drop center velocities, are decoupled from any other equations. Similarly, the integral equations for the first-order sine coefficients for $\alpha = x$ and σ, also involving the z-components of the drop center velocity, are decoupled from any other equations.
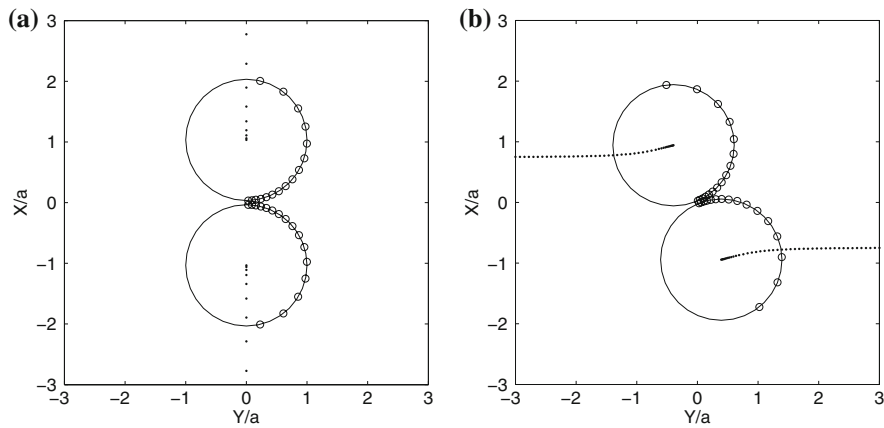
Fig. 2 Adaptive distribution of collocation points along the contours of two intercepting spherical drops according to the interfacial gap in **a** uniaxial extensional flow, and **b** simple shear flow. The *dots* trace the drop center trajectories

4 Numerical methods

To solve the integral equations derived in Sect. 3, we divide the particle contours in the $\varphi = 0$ meridional plane into circular elements and approximate the unknown Fourier coefficients with constant functions over each element. For best accuracy, the elements are concentrated near the axis of symmetry so that their length increases geometrically with distance from the axis of symmetry, shown in Fig. 2. Given the number of elements, the element stretch ratio is determined by r-adaptation, so that the size of the element in the middle of the interfacial gap is comparable to the gap size. Applying point collocation at the midpoint of each element, we generate systems of linear equations for the unknown solution vector including element values of the unknown Fourier coefficients and the Cartesian components of the drop translational velocities. The integrals over the boundary elements determining the influence coefficients are computed using the six-point Gauss–Legendre quadrature. The logarithmic singularities of the singular elements are subtracted out and computed analytically over the circular segments.

4.1 Zeroth-order Fourier coefficients

The structure of the coefficient matrix corresponding to the zero-order integral equations (3.20) and (3.21) is depicted in Fig. 3a for fluids with the same viscosity, and in Fig. 3b for fluids with arbitrary viscosities. The unknown solution vector consists of boundary-element values over the first drop (A) and second drop (B), accompanied by the x-components of the drop center velocities arranged in the following order:

$$[(\Delta \mathcal{F}_{r0})_A \quad (\Delta \mathcal{F}_{r0})_B \quad | \quad (\mathcal{U}_{\theta 0})_A \quad (\mathcal{U}_{\theta 0})_B \quad | \quad (v_x)_A \quad | \quad (v_x)_B]. \tag{4.1}$$

The last two equations set a value for the x-component of the force on each drop.

4.2 First and second-order Fourier coefficients for equal viscosities

The structure of the coefficient matrix corresponding to the integral equations for the first-order cosine or sine Fourier coefficients expressed by (3.30) or (3.31) for fluids with equal viscosity is identical to that depicted in Fig. 3a. In fact, the coefficient matrices for the cosine and sine Fourier coefficients, but not the right-hand sides, are identical.
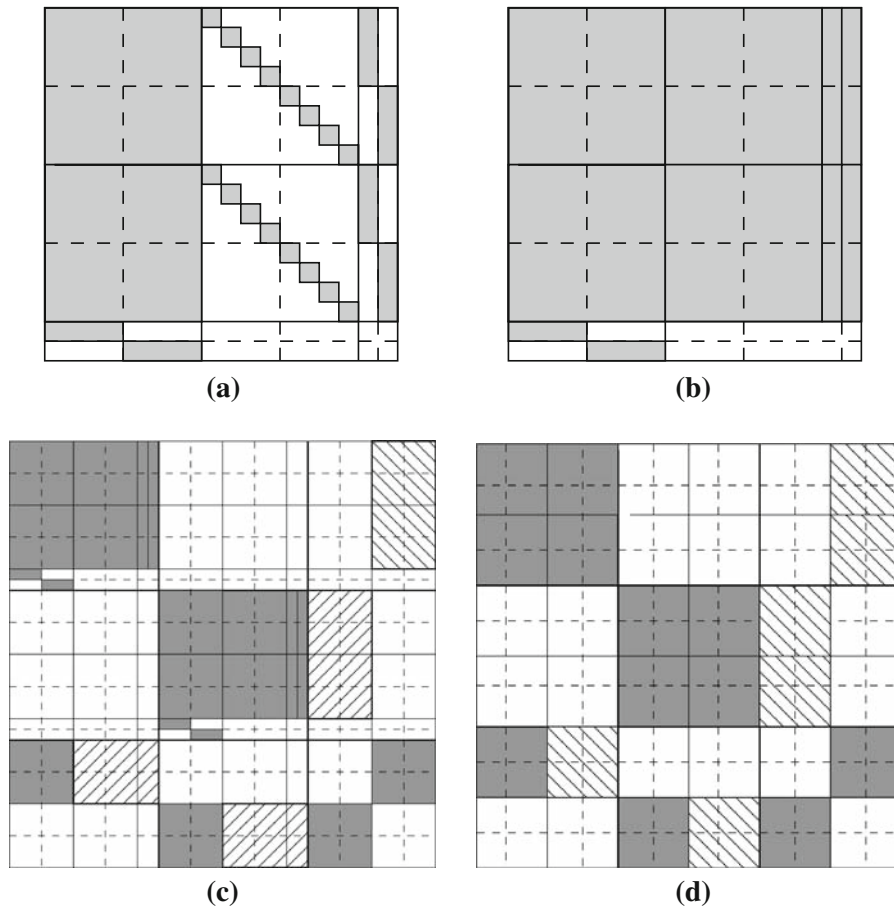
Fig. 3 Structure of the coefficient matrix corresponding to the integral equations for the constant Fourier coefficients for fluids with **a** equal viscosity, and **b** arbitrary viscosity. **c, d** Structure of the coefficient matrix corresponding for the first- and second-order Fourier coefficients for fluids with arbitrary viscosities. The *vertical dashed lines* demarcate blocks with element values for drop A or B. The *horizontal dashed lines* demarcate integral equations and force constraints for collocation points on sphere A or B

The unknown solution vector for the cosine coefficients consists of boundary-element values accompanied by the y-components of the drop center velocities arranged in the following order:

$$[(\Delta \mathcal{F}_{r1}^c)_A \quad (\Delta \mathcal{F}_{r1}^c)_B \quad | \quad (\mathcal{U}_{\theta 1}^c)_A \quad (\mathcal{U}_{\theta 1}^c)_B \quad | \quad (v_y)_A \quad | \quad (v_y)_B]. \tag{4.2}$$

The last two equations enforce the condition of zero y-component of the force on each particle. The unknown solution vector for the sine coefficients consists of boundary-element values accompanied by the z-components of the drop center velocities arranged in the following order:

$$[(\Delta \mathcal{F}_{r1}^s)_A \quad (\Delta \mathcal{F}_{r1}^s)_B \quad | \quad (\mathcal{U}_{\theta 1}^s)_A \quad (\mathcal{U}_{\theta 1}^s)_B \quad | \quad (v_z)_A \quad | \quad (v_z)_B]. \tag{4.3}$$

The last two equations enforce the condition of zero z-component of the force on each particle.

4.3 First and second-order Fourier coefficients for arbitrary viscosities

The structure of the coefficient matrix corresponding to the integral equations for the first-order cosine and sine Fourier coefficients for fluids with arbitrary viscosities is depicted in Fig. 3c. The unknown solution vector consists of boundary-element values accompanied by the y- and z-components of the drop center velocities arranged in the following order:

$$
\begin{aligned}
&[(\Delta\mathcal{F}_{r1}^c)_A \quad (\Delta\mathcal{F}_{r1}^c)_B \quad | \quad (\mathcal{U}_{\theta1}^c)_A \quad (\mathcal{U}_{\theta1}^c)_B \quad | \quad (v_y)_A \quad | \quad (v_y)_B \quad | \\
&\quad (\Delta\mathcal{F}_{r1}^s)_A \quad (\Delta\mathcal{F}_{r1}^s)_B \quad | \quad (\mathcal{U}_{\theta1}^s)_A \quad (\mathcal{U}_{\theta1}^s)_B \quad | \quad (v_z)_A \quad | \quad (v_z)_B \quad | \\
&\quad (\mathcal{U}_{\varphi1}^c)_A \quad (\mathcal{U}_{\varphi1}^c)_B \quad | \quad (\mathcal{U}_{\varphi1}^s)_A \quad (\mathcal{U}_{\varphi1}^s)_B].
\end{aligned}
\tag{4.4}
$$

Four equations enforce the condition of zero y- and z-components of the force on each drop. The first diagonal block is identical to the second diagonal block, and the northeastern off-diagonal block is the negative of the southwestern off-diagonal block. The hatched blocks depicted in Fig. 3c become null when the fluid viscosities are equal, and this allows the decoupling of the diagonal blocks, as shown in Fig. 3a.

The structure of the coefficient matrix corresponding to the integral equations for the second-order cosine and sine Fourier coefficients for fluids with arbitrary viscosities is depicted in Fig. 3d. The unknown solution vector consists of boundary-element values arranged in the following order:

$$
\begin{aligned}
&[(\Delta\mathcal{F}_{r2}^c)_A \quad (\Delta\mathcal{F}_{r2}^c)_B \quad | \quad (\mathcal{U}_{\theta2}^c)_A \quad (\mathcal{U}_{\theta2}^c)_B \quad | \quad (\Delta\mathcal{F}_{r2}^s)_A \quad (\Delta\mathcal{F}_{r2}^s)_B \quad | \\
&\quad (\mathcal{U}_{\theta2}^s)_A \quad (\mathcal{U}_{\theta2}^s)_B \quad | \quad (\mathcal{U}_{\varphi1}^c)_A \quad (\mathcal{U}_{\varphi1}^c)_B \quad | \quad (\mathcal{U}_{\varphi1}^s)_A \quad (\mathcal{U}_{\varphi1}^s)_B].
\end{aligned}
\tag{4.5}
$$

The solution does not involve, and is independent of the drop center velocities.

4.4 Drop motion

The equations of (2.33) governing the droplet motion were integrated in time using the second-order Runge–Kutta method. When the particle gap is small, large lubrication forces develop rendering the differential equations stiff and raising the possibility of unnatural collision and artificial overlap at a finite time. To ensure a regular behavior, the time step is adjusted according to the particle gap, ϵ, and the relative particle velocity in the laboratory frame, as $\Delta t = \omega\epsilon/|\mathbf{V}^A - \mathbf{V}^B|$, where ω is a numerical coefficient. This time step is accepted only if it is lower than a specified value, Δt_0, used for well-separated particles.

5 Stresslet and particle stress tensor

The disturbance flow far from the droplets is induced by a stresslet with strength

$$
\begin{aligned}
s_{ij} = \frac{1}{2} \iint_{\mathcal{D}_1} [x_i\,\Delta f_j^D + x_j\,\Delta f_i^D - 2\,(\mu_1 - \mu_2)\,(u_i n_j + u_j n_i)\,]\,\mathrm{d}S \\
+ \frac{1}{2} \iint_{\mathcal{D}_2} [x_i\,\Delta f_j^D + x_j\,\Delta f_i^D - 2\,(\mu_1 - \mu_3)\,(u_i n_j + u_j n_i)\,]\,\mathrm{d}S;
\end{aligned}
\tag{5.1}
$$

e.g., [15, p. 48]. Note that, in the case of freely convected droplets, the integral remains unchanged when the origin is shifted to a new location. In compact form,

$$
s_{ij} = \mathcal{J}_{ij}(\Delta\mathbf{f}^D; \mathcal{D}_1, \mathcal{D}_2) - \frac{2}{a}\,(\mu_1 - \mu_2)\,\mathcal{J}_{ij}(\mathbf{u}; \mathcal{D}_1) - \frac{2}{\delta a}\,(\mu_1 - \mu_3)\,\mathcal{J}_{ij}(\mathbf{u}; \mathcal{D}_2),
\tag{5.2}
$$

where

$$
\mathcal{J}_{ij}(\mathbf{f}; \mathcal{R}) = \frac{1}{2} \iint_{\mathcal{R}} (n_i\,f_j + n_j\,f_i)\,\mathrm{d}S.
\tag{5.3}
$$

Substituting the Fourier expansions and performing the integration with respect to the meridional angle, φ, we obtain

$$\mathcal{J}_{xx}(\mathbf{f}; \mathcal{R}) = 2\pi \int_C \widetilde{x} \, \mathcal{F}_{x0} \, \sigma \, \mathrm{d}l, \quad \mathcal{J}_{xy}(\mathbf{f}) = \frac{\pi}{2} \int_C [\widetilde{x} \, (\mathcal{F}_{\sigma 1}^c - \mathcal{F}_{\varphi 1}^s) + \sigma \, \mathcal{F}_{x1}^c] \, \sigma \, \mathrm{d}l,$$

$$\mathcal{J}_{xz}(\mathbf{f}; \mathcal{R}) = \frac{\pi}{2} \int_C [\widetilde{x} \, (\mathcal{F}_{\sigma 1}^s + \mathcal{F}_{\varphi 1}^c) + \sigma \mathcal{F}_{x1}^s] \, \sigma \, \mathrm{d}l,$$

$$\mathcal{J}_{yy}(\mathbf{f}; \mathcal{R}) = \pi \int_C (\mathcal{F}_{\sigma 0} + \frac{1}{2} \mathcal{F}_{\sigma 2}^c - \frac{1}{2} \mathcal{F}_{\varphi 2}^s) \, \sigma^2 \, \mathrm{d}l, \tag{5.4}$$

$$\mathcal{J}_{yz}(\mathbf{f}; \mathcal{R}) = \frac{\pi}{2} \int_C (\mathcal{F}_{\varphi 2}^c + \mathcal{F}_{\sigma 2}^s) \, \sigma^2 \, \mathrm{d}l,$$

$$\mathcal{J}_{zz}(\mathbf{f}; \mathcal{R}) = \pi \int_C (\mathcal{F}_{\sigma 0} - \frac{1}{2} \mathcal{F}_{\sigma 2}^c + \frac{1}{2} \mathcal{F}_{\varphi 2}^s) \, \sigma^2 \, \mathrm{d}l,$$

where C is the contour of the spherical surface $\mathcal{R}$ in a meridional plane, $\widetilde{x} = x - x_c$, and x_c is the axial position of the spherical surface. These expressions reveal that the off-diagonal components of the stresslet depend on the zeroth and first Fourier coefficients, while the diagonal components depend on the zeroth, first and second Fourier coefficients.

Using the rules of tensor transformation, we find that the stresslet in the laboratory frame is given by

$$\mathbf{S} = \mathbf{A} \cdot \mathbf{s} \cdot \mathbf{A}^T. \tag{5.5}$$

The dimensionless particle stress tensor is defined as

$$\mathbf{\Sigma}^p = \frac{1}{\mu_1 k 4\pi (V_{p1} + V_{p2})} \, \mathbf{S}, \tag{5.6}$$

where k is an appropriate constant shear or extensional rate, and V_{p1}, V_{p2} are the particle volumes.

Batchelor [16] showed that the effective stress tensor of a suspension of force-free spherical particles or liquid droplets freely convected in infinite linear flow is given by

$$\mathbf{\Sigma}^{\mathrm{eff}} = \mu_1 \left(2 \mathbf{E}^\infty + \frac{1}{V} \mathbf{S} \right), \tag{5.7}$$

where $\mathbf{E}^\infty$ is the rate-of-deformation tensor of the linear flow, and $\mathbf{S}$ is the stresslet computed over the surfaces of all particles in a given volume, V. In the limit of infinite dilution, $\mathbf{S} \simeq n \, \mathbf{S}^1$, where $\mathbf{S}^1$ is the stresslet computed over the surface of one particle, and n is the particle number density defined as the number of particles in the given volume V, divided by V. Thus,

$$\mathbf{\Sigma}^{\mathrm{eff}} \simeq \mu_1 \left(2 \mathbf{E}^\infty + \frac{n}{V} \mathbf{S}^1 \right) \equiv \mu_1 \left(2 \mathbf{E}^\infty + ck \, \mathbf{\Sigma}^{p1} \right), \tag{5.8}$$

where $c = n V_p$ is the particle volume fraction;

$$\mathbf{\Sigma}^{p1} \equiv \frac{1}{\mu_1 k V_p} \mathbf{S}^1 \tag{5.9}$$

is the one-particle stress tensor and V_p is the volume of one particle. A detailed calculation shows that

$$\mathbf{\Sigma}^{p1} = \frac{\alpha_1}{k} \, 2\mathbf{E}^\infty, \tag{5.10}$$

and thus

$$\mathbf{\Sigma}^{\mathrm{eff}} \simeq \mu_1 \, (1 + \alpha_1 \, c) \, 2\mathbf{E}^\infty, \tag{5.11}$$

where α_1 is a constant. Thus, a dilute suspension of spherical particle behaves like a Newtonian fluid with elevated viscosity. For rigid particles with no-slip surfaces, Einstein [17] calculated $\alpha_1 = 5/2$. For spherical drops enclosing a fluid with viscosity $\lambda\mu_1$, Taylor [14] calculated

$$\alpha_1 = \frac{1}{2}\frac{5\lambda + 2}{\lambda + 1}. \tag{5.12}$$

The Einstein value arises in the limit $\lambda \to \infty$.

6 Droplet interception in uniaxial extensional flow

In the case of axisymmetric uniaxial extensional flow where the fluid approaches the origin along the X-axis and departs along the Y- and Z-axes, the velocity components in the laboratory frame are $U_X^\infty = -2kX$, $U_Y^\infty = kY$, and $U_Z^\infty = kZ$, and the associated velocity gradient tensor is

$$\mathbf{L} = k \begin{bmatrix} -2 & 0 & 0 \\ 0 & 1 & 0 \\ 0 & 0 & 1 \end{bmatrix}, \tag{6.1}$$

where k is a constant rate of extension with dimensions of inverse time. In this section, we consider situations where the drops are placed and convected along the X-axis toward the origin in a collision course.

Figure 4 shows results of computations for two identical drops with the same viscosities, $\delta = 1$ and $\mu_2 = \mu_3$, positioned symmetrically with respect to the origin, $X_B = -X_A$. The left column shows graphs of the lower drop center velocity plotted against the interfacial gap scaled by the drop radius, $\xi = \epsilon/a$, on a log-log scale. Results are shown for three viscosity ratios, $\lambda \equiv \mu_2/\mu_1 = \mu_3/\mu_1 = 0.01$, 1, and 100. The various symbols correspond to simulations with an increasing number of boundary elements adaptively distributed over the spherical interfaces according to the interfacial gap, as discussed in Sect. 4. The finest computation with 128 boundary elements along each drop contour produces accurate results for gaps as small as 10^{-4} times the drop radius. When the fluid viscosities are equal, the finest simulation requires less than one hour of CPU time on a high-end personal computer. When the fluid viscosities are different, the finest simulation requires several hours of CPU time.

The initial stage of the motion for remote drops involves weak far-field hydrodynamic interactions where the drops act like potential and point-force dipoles. The second stage of the motion for closely spaced drops is dominated by strong hydrodynamic interactions. Given the drop center position, the drop velocity monotonically increases as the drop viscosity is raised and reaches a maximum when the drops reduce to rigid particles. As the interfaces tend to touch, the drop center velocity evolves according to the scaling law $V_x \simeq kac\,\xi^m$, where m is a positive exponent strongly dependent on the viscosity ratio, λ, and c is a constant. Thus, as the interfaces touch, the drop collision velocity tends to zero.

The slope of the dotted line in each frame of the left column of Fig. 4 is equal to unity. The results reveal that the exponent m is less than unity for any finite value of λ, and tends to the value of unity in the limit of spherical solid particles as λ tends to infinity. These observations will be supported by independent evidence discussed later in this section. Integrating the equation $\mathrm{d}\xi/\mathrm{d}(kt) = -c\,\xi^m$, we find that, if $m = 1$, the gap decreases exponentially in time and closes after an infinite collision time; whereas, if $m < 1$, the gap closes after a finite collision time. These considerations confirm that spherical drops and bubbles coalesce after a finite evolution time, whereas rigid particles never touch. However, strong lubrication forces develop for small interfacial gaps on the order of Ca, as shown in Fig. 5a, and the assumption of a perfectly spherical shape ceases to be accurate after a certain stage during the interception. In practice, the drops coalesce when the minimum film thickness between the spherical interfaces is below a threshold where attractive intermolecular forces arise leading to rupture.

The deformation of the interfaces to leading-order with respect to the capillary number is described by the function $\phi(\theta)$ introduced in Sect. 2, defined such that the drop radius is $r = R[1 + \mathrm{Ca}\,\phi(\theta)]$. In the case of uniaxial extensional flow, the function $\phi(\theta)$ satisfies the ordinary differential equation

$$\frac{\mathrm{d}^2\phi}{\mathrm{d}\theta^2} + \cot\theta\,\frac{\mathrm{d}\phi}{\mathrm{d}\theta} + 2\phi = -\frac{R}{\mu_1 U}\,\Delta\mathcal{F}_{r0} + c, \tag{6.2}$$
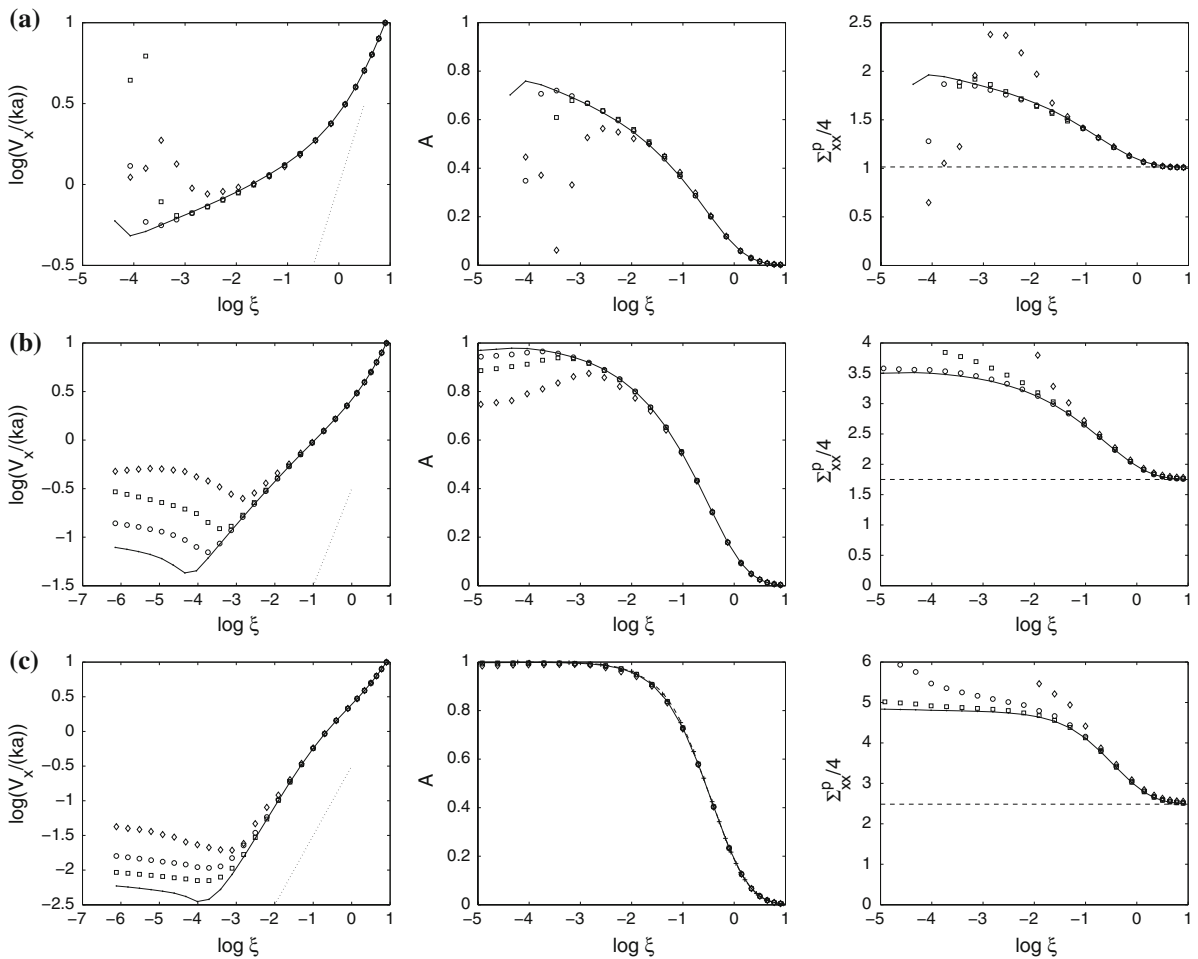
Fig. 4 Two identical drops with the same viscosity collide in uniaxial extensional flow. The *graphs* illustrate the dependence of the axial drop center velocity (*left*), axial particle mobility coefficient, $\mathcal{A}$ (*middle*), and xx-component of the particle stress tensor (*right*), on the scaled interfacial gap, ξ, for **a** $\lambda \equiv \mu_2/\mu_1 = \mu_3/\mu_1 = 0.01$, **b** $\lambda = 1$, and **c** $\lambda = 100$. The *dots*, *circles*, *squares*, *diamonds*, and *crosses* correspond, respectively, to 16, 32, 64, and 128 elements around each spherical interface. The slope of the *dotted lines* in the left frames is equal to unity. The *dashed horizontal lines* in the right frames represent the Taylor value for a solitary drop

originating from (2.19), subject to the boundary condition $\mathrm{d}\phi/\mathrm{d}\theta = 0$ at $\theta = 0$ and π. In light of the non-uniqueness of the integral equations for $\Delta\mathcal{F}_{r0}$, the constant c is adjusted so that the drop volume is preserved to leading order with respect to Ca, by requiring

$$\int_0^\pi \phi(\theta) \sin^3\theta \, \mathrm{d}\theta = 0. \tag{6.3}$$

Equation 6.2 was solved using a standard second-order finite-difference method on a grid defined by the boundary-element nodes. Deformed interfacial profiles for an arbitrary capillary number are shown in Fig. 5b. A familiar axisymmetric dimple develops at the point of contact identified as a lubrication zone.

A dimensionless axial relative mobility coefficient can be defined in terms of the scaled difference between the actual drop velocity and the velocity of the extensional flow evaluated at the instantaneous drop center,
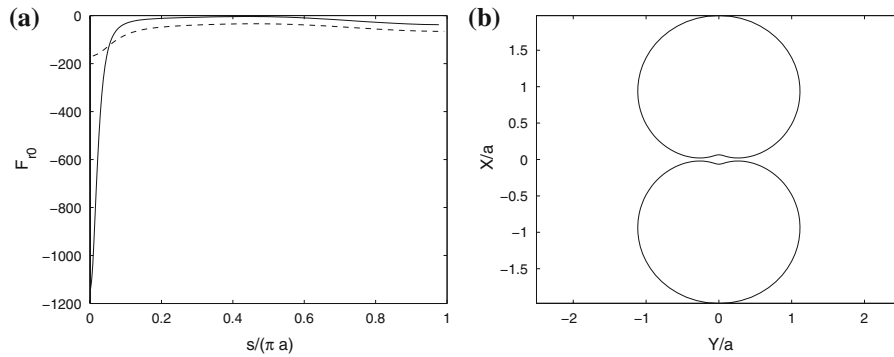
$$\mathcal{A} = 1 + \frac{V_X}{2kX}. \tag{6.4}$$

Fig. 5 **a** Interception of two identical drops with the same viscosity in uniaxial extensional flow: distribution of the jump in the interfacial traction scaled by $k\mu_1$, plotted with respect to arc length measured around the drop contour for interfacial gap $\xi = 0.1$ (*dashed line*) and 0.01 (*solid line*). **b** Deformed interfacial profiles for $\xi = 0.01$ and $Ca = 0.01$

Fig. 6 Dependence of the dimensionless axial relative mobility coefficient, $\mathcal{A}$, on the scaled gap between two identical drops, ξ, for viscosity ratio $\lambda = 0.01$ (*circles*), 1 (*squares*), and 100 (*diamonds*). *The crosses* represent data of Batchelor and Green [2], and *the dashed lines* represent a numerical approximation for solid spherical particles
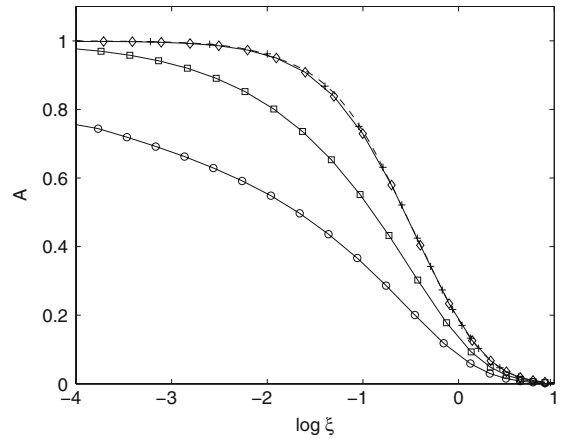
As the distance between the drops becomes larger, hydrodynamic interactions become increasingly weak and $\mathcal{A}$ tends to zero. In the opposite limit where the gap tends to zero, the drop velocity tends to zero and $\mathcal{A}$ tends to unity. Graphs of the function $\mathcal{A}(\xi)$ are shown in the middle column of Fig. 4 for several discretization levels and three viscosity ratios, and a summary of the most accurate results is given in Fig. 6. The boundary-integral computations are in excellent agreement with results presented in [9, Fig. 2c], obtained by asymptotic and functional expansion methods. The results for $\lambda = 100$ are in excellent agreement with data given in [2, Table 1] for solid particles represented by the crosses, corresponding to infinite viscosity ratio.

Da Cunha and Hinch [18] provide approximate expressions for the function $\mathcal{A}$ in the case of identical solid particles. In the far field, $r \geq 2.5$,

$$\mathcal{A} = \frac{5}{r^3} - \frac{8}{r^5} + \frac{25}{r^6} - \frac{35}{r^8} + \frac{125}{r^9} - \frac{102}{r^{10}} + \frac{12.5}{r^{11}} + \frac{430}{r^{12}}. \tag{6.5}$$

In the intermediate regime, $2.01 < r < 2.5$,

$$\mathcal{A} = -4.3833 + \frac{17.7176}{r} + \frac{14.8204}{r^2} - \frac{92.4471}{r^3} - \frac{46.3151}{r^4} + \frac{232.2304}{r^5}. \tag{6.6}$$

In the lubrication regime, $2 < r \leq 2.01$,

$$\mathcal{A} = \frac{16.3096}{r} - 7.1548, \tag{6.7}$$

where $r = 2 + \xi$ is the scaled distance between the particle centers. The predictions of these formulas are represented by the dashed line in Fig. 6 and in the middle frame of Fig. 4c. As ξ tends to zero, $\mathcal{A} \simeq 1 - \frac{1}{2} 8.3096 \, \xi$, and $V_X \sim \xi$, in agreement with the numerical results presented in the left frame of Fig. 4c.

The right column in Fig. 4 shows graphs of the xx-component of the particle stress tensor plotted against the interfacial gap on a log-linear scale. The results show that the particle stress tensor increases monotonically from the Taylor value α_1 given in (5.12) for well separated particles represented by the horizontal lines, to a higher finite value in the limit of vanishing gap. The limiting value for zero gap is at least twice the Taylor value for all viscosity ratios. Thus, drop interception considerably increases the effective extensional viscosity of a dilute suspension.

7 Droplet interception in simple shear flow

In the case of simple shear flow along the Y-axis with velocity varying linearly along the X-axis, the velocity components in the laboratory frame are $U_X^\infty = 0$, $U_Y^\infty = kX$, and $U_Z^\infty = 0$, and the associated velocity gradient tensor is

$$\mathbf{L} = k \begin{bmatrix} 0 & 1 & 0 \\ 0 & 0 & 0 \\ 0 & 0 & 0 \end{bmatrix}, \tag{7.1}$$

where k is the shear rate. Making substitutions, we derive the streaming component of the incident flow in the droplet doublet frame,

$$v_x^\infty = A_{Yx} \, X_c^{(1)}, \quad v_y^\infty = A_{Yy} \, X_c^{(1)}, \quad v_z^\infty = A_{Yz} \, X_c^{(1)}, \tag{7.2}$$

and the associated velocity gradient tensor,

$$\mathbf{M}^T = k \begin{bmatrix} A_{Yx}A_{Xx} & A_{Yx}A_{Xy} & A_{Yx}A_{Xz} \\ A_{Yy}A_{Xx} & A_{Yy}A_{Xy} & A_{Yy}A_{Xz} \\ A_{Yz}A_{Xx} & A_{Yz}A_{Xy} & A_{Yz}A_{Xz} \end{bmatrix} = k \, \mathbf{r_2} \otimes \mathbf{r_1}, \tag{7.3}$$

where $\mathbf{r}_1$ and $\mathbf{r}_2$ are the first and second rows of $\mathbf{A}$. When the axis connecting the drop centers lies in the XY-plane, yielding a flow with planar symmetry, we set $A_{Zx} = 0$ for the first unit vector, $A_{Xy} = -A_{Yx}$, $A_{Yy} = A_{Xx}$, $A_{Zy} = 0$ for the second unit vector, and $A_{Xz} = 0$, $A_{Yz} = 0$, $A_{Zz} = 1$ for the third unit vector, and find that the last row and column of the matrix $\mathbf{M}$ are zero. Accordingly,

$$\mathbf{M}^T = k \begin{bmatrix} M_{11} & M_{12} - 1 & 0 \\ M_{12} & -M_{11} & 0 \\ 0 & 0 & 0 \end{bmatrix} \tag{7.4}$$

and

$$u_x^\infty = v_x^\infty + kM_{11} \, x + k(M_{12} - 1) \, y, \quad u_y^\infty = v_y^\infty + kM_{12} \, x - kM_{11} \, y, \quad u_z^\infty = 0, \tag{7.5}$$

where $M_{11} = A_{Xx}A_{Yx}$ and $M_{12} = A_{Xx}^2$.

To develop insight into the drop motion and simultaneously assess the performance of the numerical method, we consider the interception of two identical drops whose viscosity is equal to that of the ambient fluid, $\mu_2 = \mu_3 = \mu_1$. At the initial instant, the drop centers reside in the XY-plane at positions $\mathbf{X}_A = (0.75, -3, 0)a$ and $\mathbf{X}_B = (-0.75, 3, 0)a$. Figure 7a shows the trajectories of the drop centers in the XY-plane computed using far-field
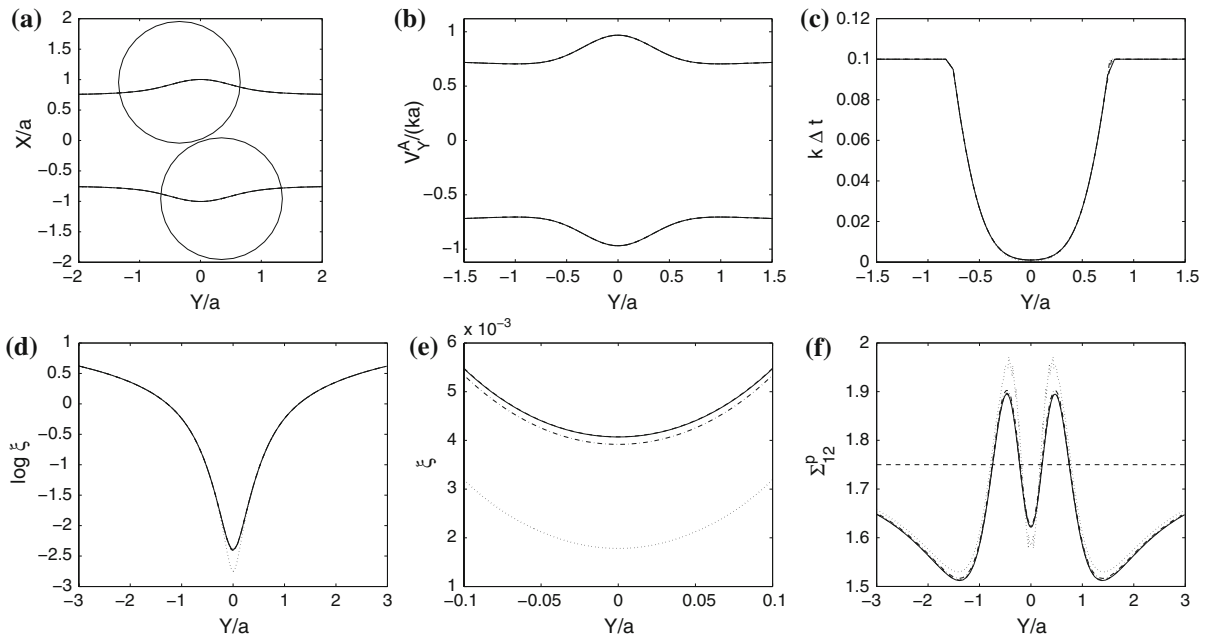
Fig. 7 **a** Trajectories of two identical drops with the same viscosity in the XY-plane for initial drop center position $\mathbf{X}_A = (0.75, -3, 0)a$ and $\mathbf{X}_B = (-0.75, 3, 0)a$. **b** Streamwise drop velocities, and **c** adaptive evolution of the time step according to the inter-particle gap. **d, e** Evolution of the gap between the interfaces plotted on a logarithmic or linear scale. **f** Evolution of the shearing component of the particle stress tensor. The *dotted*, *dot-dashed*, *dashed*, and *solid lines* represent the results of computations with 16, 32, 64, and 128 boundary elements around each drop contour in a meridional plane

time step $k\Delta t_0 = 0.10$ and relaxation parameter $\omega = 0.5$. Drop contours at an arbitrary time instant are shown to demonstrate the close proximity of the interfaces. The hardly distinguishable dotted, dot-dashed, dashed, and solid lines represent the results of computations with 16, 32, 64, and 128 boundary elements around each drop contour in a meridional plane. The results reveal that the drops intercept, nearly collide, rotate as a doublet about the origin, and then separate to resume their rectilinear path. A net lateral displacement does not occur due to reversibility of Stokes flow. Figure 7b shows that, in fact, the drops accelerate in the streamwise direction as they are pushed upward or downward during the interception.

Very small gaps separate the interfaces during the interception, requiring correspondingly small time steps, as shown in Fig. 7c. Figure 7d and e describes the evolution of the minimum gap between the interfaces. The results uniformly converge as the number of boundary elements is doubled. The interfacial gap is drastically reduced by nearly two orders of magnitude as the drops nearly collide. The minimum gap occurs in the vertical orientation along the X-axis and is on the order of 10^{-3} times the drop radius. The calculation with 64 boundary elements accurately describes the drop motion at near contact. Figure 7f describes the evolution of the shearing component of the particle stress tensor expressing the contribution of the drops to the effective viscosity of the suspension. When the drops are well-separated, we obtain Taylor's value for solitary drops, $\Sigma_{XY}^{p1} = 1.75$. It is interesting that particle interception causes strong oscillations that may temporarily reduce the effective viscosity of the suspension below the single-particle value corresponding to infinite dilution.

Figure 8 describes the evolution of the gap and shearing component of the particle stress tensor for two identical drops with unit viscosity ratio initially positioned at $Y_A = -3a$ and $Y_B = 3a$, and three initial lateral positions, $Y_A = -Y_B = 0.70a, 0.75a$, and $0.80a$. In Fig. 8a, the logarithm of the gap is plotted against the longitudinal position of the first particle, Y_A. The simulations demonstrate that, when the initial offset is sufficiently small, the interfaces come in contact after a finite evolution time, in agreement with the results of Wang et al. [9]. Figure 8b
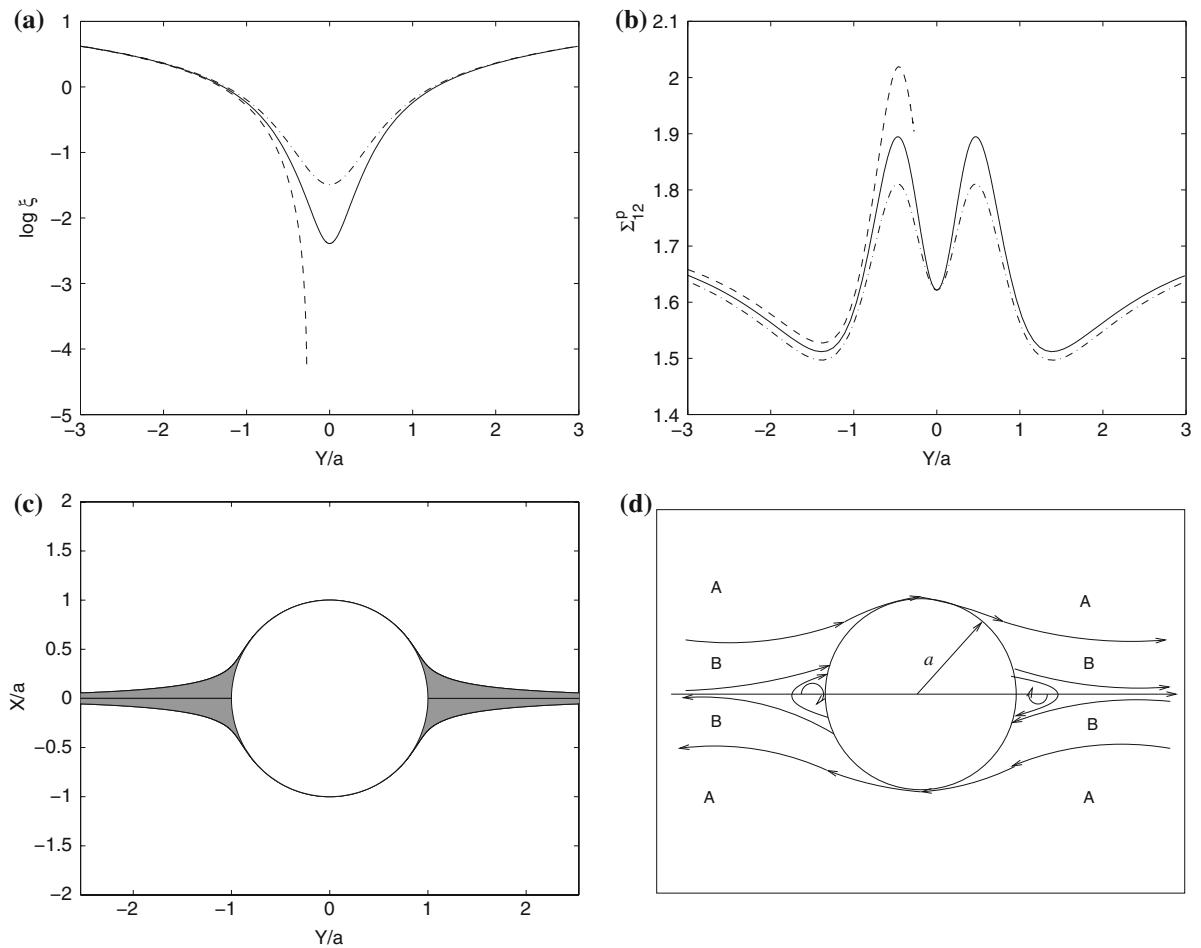
Fig. 8 a Effect of the initial lateral drop position on the evolution of the minimum gap between two spherical drops intercepting in the (X, Y) plane, and **b** associated shearing component of the particle stress tensor. **c** Relative motion of two identical spherical solid particles: initial particle center positions in the (X, Y) plane symmetrically positioned with respect to the origin inside the *shaded area* lead to closed particle trajectories. **d** Schematic illustration of the relative motion of two identical spherical liquid drops after Wang et al. [9]. Drop whose centers are located in region A roll over one another following open trajectories; drops whose centers are located in region B either collide or undergo a perpetual orbiting motion

shows that the particle stress tensor remains finite even when the interfaces come in contact. We conclude that drop collision does not have a profound effect on the rheology of a dilute suspension.

Batchelor and Green [2] pointed out that two intercepting solid particles never collide, as strong lubrication forces developing in narrow gaps resist normal motion. However, not all relative particle trajectories originate from infinity, as illustrated in Fig. 8c for identical particles. Initial particle center positions symmetrically located with respect to the origin inside the shaded area lead to closed trajectories where the particles exhibit a perpetual orbiting motion. When the particle centers are initially located at the horizontal Y-axis, they spontaneously migrate off the axis and nearly touch when they reach the vertical orientation along the X-axis, but never collide. Wang et al. [9] found that the relative trajectories of spherical liquid drops involve a roll-over zone (A) and a collision zone (B) where the interfaces come into physical contact, as illustrated in Fig. 8d. Closed trajectories representing a perpetual orbiting motion may arise inside the collision zone depending the relative particle radii and viscosity.

Next, we consider a pair of identical drops with the same viscosity located along the X-axis and convected along the Y-axis under the action of a simple shear flow. The dimensionless transverse relative mobility coefficient is

Fig. 9 Dependence of the
dimensionless transverse
relative mobility coefficient,
$\mathcal{B}$, on the scaled gap
between two identical
drops, ξ, for viscosity ratio
$\lambda = 1$ (*circles*), 5 (*squares*),
and 100 (*diamonds*). The
crosses represent data of
Batchelor and Green [2],
and the *dashed lines*
represent a numerical
approximation for spherical
solid particles. As ξ tends to
zero, $\mathcal{A}$ tends to a limit that
is less than unity in all cases
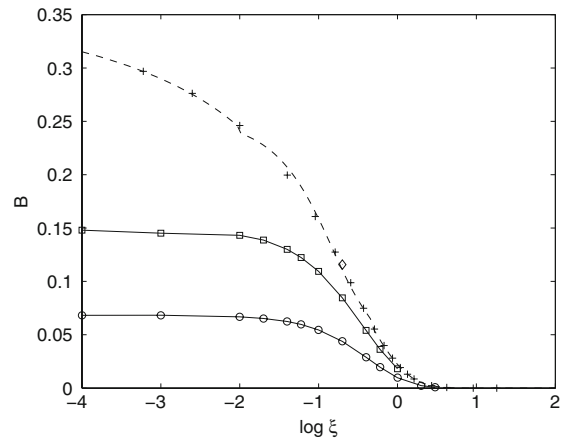
defined in terms of the scaled difference between the actual drop velocity along the Y-axis, and the velocity of the simple shear flow evaluated at the instantaneous drop center,

$$\mathcal{B} \equiv 2 \left(1 - \frac{V_Y}{kX} \right). \tag{7.6}$$

As the distance between the drops becomes larger, hydrodynamic interactions become weaker and $\mathcal{B}$ tends to zero. In the opposite limit where the gap tends to zero, the drop velocity tends to a nonzero value and $\mathcal{B}$ tends to a nonzero limit. Graphs of the function $\mathcal{B}(\xi)$ computed with 128 boundary elements plotted against the scaled gap, ξ, are shown in Fig. 9. The results are in excellent agreement with graphs presented in [9, Fig. 3c], obtained by asymptotic and functional expansion methods. Excellent agreement is also observed with data for spherical solid particles provided by Batchelor and Green [2] corresponding to infinite viscosity ratio, represented by the crosses. As ξ tends to zero, the function $\mathcal{B}$ tends to a finite value that is lower than unity for any viscosity ratio, including infinity. Thus, solid particles and liquid drops are able to tangentially roll over one another and separate under the action of a simple shear flow.

Da Cunha and Hinch [18] provide approximate expressions for the function $\mathcal{B}$ in the case of identical solid particles. In the far field, $r \geq 2.5$,

$$\mathcal{B} = \frac{1}{3} \left(\frac{16}{r^5} + \frac{10}{r^8} - \frac{36}{r^{10}} - \frac{25}{r^{11}} - \frac{36}{r^{12}} \right), \tag{7.7}$$

in the intermediate regime, $2.01 < r < 2.5$,

$$\mathcal{B} = -3.1918 + \frac{12.3641}{r} + \frac{11.4615}{r^2} - \frac{65.2926}{r^3} - \frac{36.4909}{r^4} + \frac{154.8074}{r^5}, \tag{7.8}$$

and in the lubrication regime, $2 < r \leq 2.01$,

$$\mathcal{B} = \frac{2}{r} \frac{0.4056 \log^2 \xi - 1.49681 \log \xi - 1.9108}{\log^2 \xi - 6.04250 \log \xi + 6.32549}, \tag{7.9}$$

where $r = 2 + \xi$ is the scaled distance between the particle centers. As the gap ξ tends to zero, $\mathcal{B}$ tends to 0.4056. The predictions of these approximations are shown with the dashed lines in Fig. 9.

8 Discussion

We have developed a numerical method for computing with high accuracy linear flow past a pair of spherical drops with arbitrary radii and viscosity. A key step is the Fourier expansion of flow variables with respect to the meridional angle measured around the axis connecting the particle centers at every instant. We have found that only the zeroth- and first-order Fourier coefficients are necessary for computing the drop center velocities. The boundary-integral formulation culminates in systems of one-dimensional integral equations that can be solved efficiently even for very small interfacial gaps. We have presented sample numerical results to illustrate the performance of the method and ensure agreement with the calculations of previous authors.

Batchelor and Green [2] demonstrated that the velocity of one freely suspended drop relative to the velocity of a second freely suspended drop intercepting in linear flow is given by

$$\mathbf{V}_A - \mathbf{V}_B = \mathbf{\Omega}^\infty \times \mathbf{r} + \mathbf{E}^\infty \cdot \mathbf{r} - \left(\frac{\mathcal{A}(s)}{r^2} \mathbf{r}\mathbf{r} + \frac{\mathcal{B}(s)}{r^2} \left(r^2 \mathbf{I} - \mathbf{r}\mathbf{r} \right) \right) \cdot \mathbf{E}^\infty \cdot \mathbf{r}, \tag{8.1}$$

where $\mathbf{r}$ is the distance between the drop centers, $s = 2r/[a(1 + \delta)]$ is the scaled dimensionless distance, $\mathbf{\Omega}^\infty$ is half the vorticity vector, and $\mathbf{E}^\infty$ is the constant rate-of-deformation tensor of the linear flow. The dimensionless axial and transverse relative mobility, functions $\mathcal{A}$ and $\mathcal{B}$, are presented in Figs. 6 and 9. Asymptotic expressions and accurate numerical values for $\mathcal{A}$ and $\mathcal{B}$ for spherical drops with the same viscosity were presented by Zinchenko, Davis and coworkers over a wide range of interfacial separations, drop to ambient fluid viscosity ratios, and drop radii ratios (e.g., [8]). The integral formulation proposed in this paper offers an alternative venue for evaluating these functions for drops with the same or different viscosities. Once these functions are available in tabular or another convenient form, studies of collision efficiency can be conducted with applications in flow-induced flotation and flocculation.

In summary, the integral formulation developed in this work allows the computation of the absolute drop velocities and particle stress tensor during the interception using relatively simple numerical methods.

Appendix A: single-layer kernels

The dimensionless single-layer kernels, $\mathcal{P}_{\alpha\beta\gamma}$, are

$$\mathcal{P}_{\alpha\beta 0} = \sigma \begin{bmatrix} \mathcal{I}_{10} + \hat{x}^2 \mathcal{I}_{30} & \hat{x}\,(\sigma\,\mathcal{I}_{30} - \sigma_0\,\mathcal{I}_{31}) & 0 \\ \hat{x}\,(\sigma\mathcal{I}_{31} - \sigma_0\mathcal{I}_{30}) & \mathcal{I}_{11} + (\sigma^2 + \sigma_0^2)\,\mathcal{I}_{31} - \sigma\sigma_0\,(\mathcal{I}_{32} + \mathcal{I}_{30}) & 0 \\ 0 & 0 & 2\mathcal{I}_{11} \end{bmatrix}, \tag{A.1}$$

$$\mathcal{P}_{\alpha\beta 1} = \sigma \begin{bmatrix} \mathcal{I}_{11} + \hat{x}^2\mathcal{I}_{31} & \hat{x}\,(\sigma\,\mathcal{I}_{31} - \sigma_0\mathcal{I}_{32}) \\ \hat{x}\,(\sigma\mathcal{I}_{32} - \sigma_0\mathcal{I}_{31}) & \mathcal{I}_{12} + (\sigma^2 + \sigma_0^2)\mathcal{I}_{32} - \sigma\sigma_0\,(\mathcal{I}_{33} + \mathcal{I}_{31}) \\ \hat{x}\sigma\,(\mathcal{I}_{32} - \mathcal{I}_{30}) & \mathcal{I}_{12} - \mathcal{I}_{10} + \sigma^2(\mathcal{I}_{32} - \mathcal{I}_{30}) - \sigma\sigma_0\,(\mathcal{I}_{33} - \mathcal{I}_{31}) \end{bmatrix}$$

$$\left. \begin{matrix} \hat{x}\sigma_0(\mathcal{I}_{32} - \mathcal{I}_{30}) \\ \mathcal{I}_{10} - \mathcal{I}_{12} + \sigma_0^2\,(\mathcal{I}_{30} - \mathcal{I}_{32}) - \sigma\sigma_0\,(\mathcal{I}_{31} - \mathcal{I}_{33}) \\ \mathcal{I}_{12} + \sigma\sigma_0\,(\mathcal{I}_{31} - \mathcal{I}_{33}) \end{matrix} \right], \tag{A.2}$$

and

$$\mathcal{P}_{\alpha\beta2} = \sigma \left[\begin{array}{c} (2\mathcal{I}_{12} - \mathcal{I}_{10}) + \hat{x}^2(2\mathcal{I}_{32} - \mathcal{I}_{30}) \\ \hat{x}\sigma\,(2\mathcal{I}_{33} - \mathcal{I}_{31}) - \hat{x}\sigma_0\,(2\mathcal{I}_{32} - \mathcal{I}_{30}) \\ 2\hat{x}\sigma\,(\mathcal{I}_{33} - \mathcal{I}_{31}) \end{array} \right. $$

$$\hat{x}\sigma\,(2\mathcal{I}_{32} - \mathcal{I}_{30}) - \hat{x}\sigma_0\,(2\mathcal{I}_{33} - \mathcal{I}_{31})$$
$$2\mathcal{I}_{13} - \mathcal{I}_{11} + (\sigma^2 + \sigma_0^2)(2\mathcal{I}_{33} - \mathcal{I}_{31}) - \sigma\sigma_0\,(2\mathcal{I}_{34} + \mathcal{I}_{32} - \mathcal{I}_{30})$$
$$2(\mathcal{I}_{13} - \mathcal{I}_{11}) + 2\sigma^2(\mathcal{I}_{33} - \mathcal{I}_{31}) - 2\sigma\sigma_0\,(\mathcal{I}_{34} - \mathcal{I}_{32})$$

$$\left. \begin{array}{c} 2\hat{x}\sigma_0(\mathcal{I}_{33} - \mathcal{I}_{31}) \\ 2(\mathcal{I}_{11} - \mathcal{I}_{13}) + 2\sigma_0^2\,(\mathcal{I}_{31} - \mathcal{I}_{33}) - 2\sigma\sigma_0\,(\mathcal{I}_{32} - \mathcal{I}_{34}) \\ (2\mathcal{I}_{13} - \mathcal{I}_{11}) + \sigma\sigma_0\,(-2\mathcal{I}_{34} + 3\mathcal{I}_{32} - \mathcal{I}_{30}) \end{array} \right], \tag{A.3}$$

where

$$\mathcal{I}_{mn} \equiv \int_0^{2\pi} \frac{\cos^n\omega\,\mathrm{d}\omega}{[\hat{x}^2 + \sigma^2 + \sigma_0^2 - 2\sigma\sigma_0\cos\omega]^{m/2}} = \frac{4w^m}{(4\sigma\sigma_0)^{m/2}} \int_0^{\pi/2} \frac{(2\cos^2\omega - 1)^n}{(1 - w^2\cos^2\omega)^{m/2}}\,\mathrm{d}\omega, \tag{A.4}$$

and $w^2 = 4\sigma\sigma_0/[\hat{x}^2 + (\sigma + \sigma_0)^2]$. These integrals can be expressed in terms of complete elliptic integrals of the first or second kind which and then evaluated either by iterative methods or by standard library functions.

When the point $\mathbf{x}_0$ lies at the surface of a sphere, as $x \to x_0$, $\sigma \to \sigma_0$ and $\theta \to \theta_0$, the diagonal components of the single-layer kernels exhibit logarithmic singularities, where θ is the meridional angle. Detailed consideration reveals

$$\begin{aligned} \mathcal{P}_{xx0} &\sim -2\log|\hat{\theta}|, \quad \mathcal{P}_{\sigma\sigma0} \sim -2\log|\hat{\theta}|, \quad \mathcal{P}_{\varphi\varphi0} \sim -4\log|\hat{\theta}|, \\ \mathcal{P}_{xx1} &\sim -2\log|\hat{\theta}|, \quad \mathcal{P}_{\sigma\sigma1} \sim -2\log|\hat{\theta}|, \quad \mathcal{P}_{\varphi\varphi1} \sim -4\log|\hat{\theta}|, \\ \mathcal{P}_{xx2} &\sim -2\log|\hat{\theta}|, \quad \mathcal{P}_{\sigma\sigma2} \sim -2\log|\hat{\theta}|, \quad \mathcal{P}_{\varphi\varphi2} \sim -3.5\log|\hat{\theta}|, \end{aligned} \tag{A.5}$$

where $\hat{\theta} = \theta - \theta_0$.

Appendix B: double-layer kernels

The double-layer kernels, $\mathcal{R}_{\alpha\beta\gamma}$, are given by

$$\mathcal{R}_{\alpha\beta0} = -6\sigma \left[\begin{array}{c} \tau\hat{x}^2\mathcal{I}_{50} - n_\sigma\sigma_0\hat{x}^2\mathcal{I}_{51} \\ \tau\hat{x}(\sigma\mathcal{I}_{51} - \sigma_0\mathcal{I}_{50}) - n_\sigma\sigma_0\hat{x}(\sigma\mathcal{I}_{52} - \sigma_0\mathcal{I}_{51}) \\ 0 \end{array} \right.$$

$$\tau\hat{x}(\sigma\mathcal{I}_{50} - \sigma_0\mathcal{I}_{51}) - n_\sigma\sigma_0\hat{x}(\sigma\mathcal{I}_{51} - \sigma_0\mathcal{I}_{52})$$
$$(\tau\sigma^2 + \tau\sigma_0^2 + n_\sigma\sigma\sigma_0^2)\mathcal{I}_{51} - n_\sigma\sigma_0(\tau + \sigma^2 + \sigma_0^2)\mathcal{I}_{52} + n_\sigma\sigma\sigma_0^2\mathcal{I}_{53} - \tau\sigma\sigma_0\mathcal{I}_{50}$$
$$0$$

$$\left. \begin{array}{c} 0 \\ 0 \\ \tau\sigma\sigma_0(\mathcal{I}_{50} - \mathcal{I}_{52}) - n_\sigma\sigma\sigma_0^2(\mathcal{I}_{51} - \mathcal{I}_{53}) \end{array} \right], \tag{B.1}$$

$$\mathcal{R}_{\alpha x1} = -6\sigma \left[\begin{array}{c} \tau\hat{x}^2\mathcal{I}_{51} - n_\sigma\sigma_0\hat{x}^2\mathcal{I}_{52} \\ \tau\hat{x}(\sigma\,\mathcal{I}_{52} - \sigma_0\mathcal{I}_{51}) - n_\sigma\sigma_0\hat{x}(\sigma\,\mathcal{I}_{53} - \sigma_0\mathcal{I}_{52}) \\ \tau\hat{x}\sigma(\mathcal{I}_{52} - \mathcal{I}_{50}) - n_\sigma\sigma\sigma_0\hat{x}(\mathcal{I}_{53} - \mathcal{I}_{51}) \end{array} \right.$$

$$\tau\hat{x}(\sigma\mathcal{I}_{51} - \sigma_0\mathcal{I}_{52}) - n_\sigma\sigma_0\hat{x}(\sigma\mathcal{I}_{52} - \sigma_0\mathcal{I}_{53})$$
$$\tau(\sigma^2 + \sigma_0^2)\mathcal{I}_{52} - \tau\sigma\sigma_0(\mathcal{I}_{53} + \mathcal{I}_{51}) - n_\sigma\sigma_0(\sigma^2 + \sigma_0^2)\mathcal{I}_{53} + n_\sigma\sigma\sigma_0^2(\mathcal{I}_{54} + \mathcal{I}_{52})$$
$$\tau\sigma^2(\mathcal{I}_{52} - \mathcal{I}_{50}) - \tau\sigma\sigma_0(\mathcal{I}_{53} - \mathcal{I}_{51}) - n_\sigma\sigma^2\sigma_0(\mathcal{I}_{53} - \mathcal{I}_{51}) + n_\sigma\sigma\sigma_0^2(\mathcal{I}_{54} - \mathcal{I}_{52})$$

$$\left. \begin{array}{c} \tau\hat{x}\sigma_0(\mathcal{I}_{52} - \mathcal{I}_{50}) - n_\sigma\sigma_0^2\hat{x}(\mathcal{I}_{53} - \mathcal{I}_{51}) \\ \tau\sigma_0^2(\mathcal{I}_{50} - \mathcal{I}_{52}) - \tau\sigma\sigma_0(\mathcal{I}_{51} - \mathcal{I}_{53}) - n_\sigma\sigma_0^3(\mathcal{I}_{51} - \mathcal{I}_{53}) + n_\sigma\sigma\sigma_0^2(\mathcal{I}_{52} - \mathcal{I}_{54}) \\ \tau\sigma\sigma_0(\mathcal{I}_{51} - \mathcal{I}_{53}) - n_\sigma\sigma\sigma_0^2(\mathcal{I}_{52} - \mathcal{I}_{54}) \end{array} \right], \tag{B.2}$$

and

$$\mathcal{R}_{\alpha x2} = -6\sigma \begin{bmatrix} \tau \hat{x}^2(2\mathcal{I}_{52} - \mathcal{I}_{50}) - n_\sigma \sigma_0 \hat{x}^2(2\mathcal{I}_{53} - \mathcal{I}_{51}) \\ \tau \hat{x}\sigma(2\mathcal{I}_{53} - \mathcal{I}_{51}) - \tau \hat{x}\sigma_0(2\mathcal{I}_{52} - \mathcal{I}_{50}) - \hat{x}n_\sigma \sigma \sigma_0(2\mathcal{I}_{54} - \mathcal{I}_{52}) \\ + \hat{x}n_\sigma \sigma_0^2(2\mathcal{I}_{53} - \mathcal{I}_{51}) \\ 2\tau \hat{x}\sigma(\mathcal{I}_{53} - \mathcal{I}_{51}) - 2\hat{x}n_\sigma \sigma \sigma_0(\mathcal{I}_{54} - \mathcal{I}_{52}) \\[6pt] \tau \hat{x}\sigma(2\mathcal{I}_{52} - \mathcal{I}_{50}) - \tau \hat{x}\sigma_0(2\mathcal{I}_{53} - \mathcal{I}_{51}) - n_\sigma \sigma \sigma_0 \hat{x}(2\mathcal{I}_{53} - \mathcal{I}_{51}) + n_\sigma \sigma_0^2 \hat{x}(2\mathcal{I}_{54} - \mathcal{I}_{52}) \\ \tau(\sigma^2 + \sigma_0^2)(2\mathcal{I}_{53} - \mathcal{I}_{51}) - \tau \sigma \sigma_0(2\mathcal{I}_{54} + \mathcal{I}_{52} - \mathcal{I}_{50}) \\ - n_\sigma \sigma_0(\sigma^2 + \sigma_0^2)(2\mathcal{I}_{54} - \mathcal{I}_{52}) + n_\sigma \sigma \sigma_0^2(2\mathcal{I}_{55} + \mathcal{I}_{53} - \mathcal{I}_{51}) \\ 2\tau \sigma^2(\mathcal{I}_{53} - \mathcal{I}_{51}) - 2\tau \sigma \sigma_0(\mathcal{I}_{54} - \mathcal{I}_{52}) - 2n_\sigma \sigma^2 \sigma_0(\mathcal{I}_{54} - \mathcal{I}_{52}) + 2n_\sigma \sigma \sigma_0^2(\mathcal{I}_{55} - \mathcal{I}_{53}) \\[6pt] 2\tau \hat{x}\sigma_0(\mathcal{I}_{53} - \mathcal{I}_{51}) - 2n_\sigma \sigma_0^2 \hat{x}(\mathcal{I}_{54} - \mathcal{I}_{52}) \\ 2\tau \sigma_0^2(\mathcal{I}_{51} - \mathcal{I}_{53}) - 2\tau \sigma \sigma_0(\mathcal{I}_{52} - \mathcal{I}_{54}) - 2n_\sigma \sigma_0^3(\mathcal{I}_{52} - \mathcal{I}_{54}) + 2n_\sigma \sigma \sigma_0^2(\mathcal{I}_{53} - \mathcal{I}_{55}) \\ \tau \sigma \sigma_0(-2\mathcal{I}_{54} + 3\mathcal{I}_{52} - \mathcal{I}_{50}) - n_\sigma \sigma \sigma_0^2(-2\mathcal{I}_{55} + 3\mathcal{I}_{53} - \mathcal{I}_{51}) \end{bmatrix},$$

$$(B.3)$$

where $\tau = n_x \hat{x} + n_\sigma \sigma$.

When the point $\mathbf{x}_0$ lies at the surface of a sphere, the components of the double-layer kernels exhibiting singular behavior are

$$\mathcal{R}_{\varphi\varphi 0} \sim \frac{6}{R}\log|\hat{\theta}|, \quad \mathcal{R}_{\varphi\varphi 1} \sim \frac{5.5}{R}\log|\hat{\theta}|, \quad \mathcal{R}_{\varphi\varphi 2} \sim \frac{5}{R}\log|\hat{\theta}|, \tag{B.4}$$

where R is the sphere radius. All other entries exhibit a regular behavior. These logarithmic singularities are consistent with the following ordering of principal-value integrals for the double-layer potential in Stokes flow: the integrand of two-dimensional flow is discontinuous along the boundary contour at the singular point; the integrand of axisymmetric flow corresponding to a Fourier expansion is logarithmically singular along the trace of the boundary in a meridional plane; and the integrand of three-dimensional flow exhibits an integrable, simple pole $(1/r)$ singularity over a locally curved surface.

References

1. Kim S, Karrila SJ (2005) Microhydrodynamics: principles and selected applications. Dover, Mineola, New York
2. Batchelor GK, Green JT (1972) The hydrodynamic interaction of two small freely-moving spheres in a linear flow field. J Fluid Mech 56:375–400
3. Batchelor GK, Green JT (1972) The determination of the bulk stress in a suspension of spherical particles to order c^2. J Fluid Mech 56:401–427
4. Zinchenko AZ (1981) The slow asymmetrical motion of two drops in a viscous medium. J Appl Math Mech 44:30–37
5. Zinchenko AZ (1983) Calculation of the effectiveness of gravitational coagulation of drops with allowance for internal circulation. J Appl Math Mech 46:58–65
6. Zinchenko AZ (1984) Hydrodynamic interaction of two identical liquid spheres in linear flow field. J Appl Math Mech 47:37–43
7. Zinchenko AZ (1984) Effect of hydrodynamic interactions between the particles on the rheological properties of dilute emulsions. Prikl Matem Mekhan 47:56–63
8. Zhang X, Davis RH (1991) The collisions of small drops due to Brownian and gravitational motion. J Fluid Mech 230:479–504
9. Wang H, Zinchenko AZ, Davis RH (1994) The collision rate of small drops in linear flow fields. J Fluid Mech 265:161–188
10. Fuentes YO, Kim S, Jeffrey DJ (1988) Mobility functions for two unequal viscous drops in Stokes flow. Part 1: axisymmetric motions. Phys Fluids 31:2445–2455
11. Fuentes YO, Kim S, Jeffrey DJ (1989) Mobility functions for two unequal viscous drops in Stokes flow. Part 2: asymmetric motions. Phys Fluids A 1:61–76
12. Zinchenko AZ, Davis RH (2005) A multipole-accelerated algorithm for close interaction of slightly deformable drops. J Comput Phys 207:695–735
13. Pozrikidis C (1997) Introduction to theoretical and computational fluid dynamics. Cambridge University Press, New York
14. Taylor GI (1932) The viscosity of a fluid containing small drops of another liquid. Proc R Soc London A 138:41–48
15. Pozrikidis C (1992) Boundary integral and singularity methods for linearized viscous flow. Cambridge University Press, New York
16. Batchelor GK (1970) The stress system in a suspension of force-free particles. J Fluid Mech 41:545–570
17. Einstein A (1906) Eine neue Bestimmung der Moleküledimensionen. Ann Phys 19:289–306
18. Da Cunha FR, Hinch EJ (1996) Shear-induced dispersion in a dilute suspension of rough spheres. J Fluid Mech 309:211–223